Measurement of the EMC effect in light and heavy nuclei

J. Arrington et al.

Measurement of the EMC effect in light and heavy nuclei

J. Arrington,[1, 2] J. Bane,[3, 4] A. Daniel,[5, 6] N. Fomin,[7, 4, 6] D. Gaskell,[8] J. Seely,[9] R. Asaturyan,[10, *]
F. Benmokhtar,[11] W. Boeglin,[12] P. Bosted,[8] M.H.S. Bukhari,[5] M.E. Christy,[13] S. Connell,[6, †] M.M. Dalton,[6, 8]
D. Day,[6] J. Dunne,[14] D. Dutta,[14, 15] L. El Fassi,[2] R. Ent,[8] H. Fenker,[8] H. Gao,[9, 15] R.J. Holt,[2] T. Horn,[11, 8, 16]
E. Hungerford,[5] M.K. Jones,[8] J. Jourdan,[17] N. Kalantarians,[5] C.E. Keppel,[8, 13] D. Kiselev,[17, ‡]
A.F. Lung,[8] S. Malace,[13] D.G. Meekins,[8] T. Mertens,[17] H. Mkrtchyan,[10] G. Niculescu,[18] I. Niculescu,[18]
D.H. Potterveld,[2] C. Perdrisat,[19] V. Punjabi,[20] X. Qian,[15] P.E. Reimer,[2] J. Roche,[8] V.M. Rodriguez,[5]
O. Rondon,[6] E. Schulte,[2] K. Slifer,[6] G.R. Smith,[8] P. Solvignon,[2, *] V. Tadevosyan,[10] L. Tang,[8, 13]
G. Testa,[17] R. Trojer,[17] V. Tvaskis,[13] F.R. Wesselmann,[6] S.A. Wood,[8] L. Yuan,[13] and X. Zheng[2, 6]

[1]*Lawrence Berkeley National Laboratory, Berkeley, California 94720, USA*
[2]*Argonne National Laboratory, Lemont, Illinois 60439, USA*
[3]*University of Massachusetts, Amherst, Massachusetts 01003, USA*
[4]*University of Tennessee, Knoxville, Tennessee 37966, USA*
[5]*University of Houston, Houston, Texas 77044, USA*
[6]*University of Virginia, Charlottesville, Virginia 22904, USA*
[7]*Los Alamos National Laboratory, Los Alamos, New Mexico 87545, USA*
[8]*Thomas Jefferson National Accelerator Facility, Newport News, Virginia 23606, USA*
[9]*Laboratory for Nuclear Science, Massachusetts Institute of Technology, Cambridge, Massachusetts 02139, USA*
[10]*A.I. Alikhanyan National Science Laboratory (Yerevan Physics Institute),*
02 Alikhanyan Brothers Str., Yerevan 0036, Armenia
[11]*University of Maryland, College Park, Maryland 20742, USA*
[12]*Florida International University, Miami, Florida 33199, USA*
[13]*Hampton University, Hampton, Virginia 23669, USA*
[14]*Mississippi State University, Mississippi State, Mississippi 39762, USA*
[15]*Triangle Universities Nuclear Laboratory, Duke University, Durham, North Carolina 27710, USA*
[16]*Catholic University of America, Washington, DC 20064, USA*
[17]*Basel University, Basel, Switzerland*
[18]*James Madison University, Harrisonburg, Virginia 22807, USA*
[19]*College of William and Mary, Wiliamsburg, Virginia, 23185, USA*
[20]*Norfolk State University, Norfolk, Virginia 23529, USA*
(Dated: December 7, 2021)

Inclusive electron scattering from nuclear targets has been measured to extract the nuclear dependence of the inelastic cross section (σ_A) in Hall C at the Thomas Jefferson National Accelerator facility. Results are presented for ^{2}H, ^{3}He, ^{4}He, ^{9}B, ^{12}C, ^{63}Cu and ^{197}Au at an incident electron beam energy of 5.77 GeV for a range of momentum transfer from Q^2=2 to 7 $(\text{GeV/c})^2$. These data improve the precision of the existing measurements of the EMC effect in the nuclear targets at large x, and allow for more detailed examinations of the A dependence of the EMC effect.

PACS numbers: 13.60.Hb,25.30.Fj,24.85.+p

I. INTRODUCTION

Quantum chromodynamics (QCD) is the theory governing the strong interaction, with quarks and gluons as elementary degrees of freedom. The interaction between quarks is mediated by gluons as the gauge bosons. Understanding QCD in terms of the elementary quark and gluon degrees of freedom remains the greatest unsolved problem of strong interaction physics. The challenge arises from the fact that quarks and gluons cannot be examined in isolation. The degrees of freedom observed in nature (hadrons and nuclei) are different from the ones typically used in the QCD formalism (quarks and gluons). However, detailed studies of the structure of hadrons, mainly protons and neutrons, provide a wealth of information on the nature of QCD. Thus, one of the main goals of the strong interaction physics is to understand how the fundamental quark and gluon degrees of freedom give rise to the nucleons and to inter-nucleon forces that bind nuclei.

The investigation of deep-inelastic scattering of leptons from the nucleon is one of the most effective ways for obtaining fundamental information on the quark-gluon substructure of the nucleon. Nuclear structure functions are sensitive the impact of the nucleon binding and motion in the nucleus, as well as possible modification to the structure of a nucleon in the nuclear medium. Measurements by the European Muon Collaboration [1] showed the unexpected result that the nuclear structure functions differed significantly from the sum of proton and neutron distributions. This observation was dubbed the 'EMC effect', and is still the focus of experimental and theoretical efforts to understand the origin of these differences in detail. We describe here an experiment where electrons were scattered from the free proton and several

---

nuclear targets to better understand the possible modification of hadron properties in the nuclear environment, with a focus on light nuclear targets.

In the remainder of this section we briefly discuss electron scattering, structure functions and introduce the kinematics. In section I, we discuss the EMC effect and briefly survey the findings of earlier experimental and theoretical investigations and discuss the physics motivation behind the present experiment. Section II gives an overview of the experimental apparatus used to collect the presented data. Section III describes the data analysis procedures and section IV discusses the details of the systematic uncertainties. The final results are presented in section V with conclusions and an overview of the results given in section VI.

A. Kinematics and definitions

Consider electron scattering off a stationary nucleon through the exchange of a single virtual photon,

$$e^-(k) + N(P) \longrightarrow e^-(k') + X \ , \qquad (1)$$

where k and k' are the four momenta of the initial and scattered electrons and P is the four momentum of the target nucleon. The four momentum of the incoming electron is $k = (E, \vec{k})$ and of the scattered electron is $k = (E', \vec{k'})$. Since the target is at rest in the laboratory frame, its four momentum is $P = (M, \vec{0})$ where M is the nucleon rest mass. Experimentally, the produced hadrons X are not detected in inclusive electron scattering. The scattering process takes place through the electromagnetic interaction by the exchange of a virtual photon γ^*, with energy, $\nu = E - E'$ and momentum $\vec{q}$. In the laboratory frame, ignoring the electron mass, one can express Q^2, the negative of the four momentum transfer squared, as $Q^2 = 4EE' \sin^2(\theta/2)$, where θ is the electron scattering angle in the lab frame, and the invariant mass of the final hadronic system as $W = \sqrt{M^2 + 2M\nu - Q^2}$. The Bjorken scaling variable, $x = Q^2/2M\nu$, represents the longitudinal momentum fraction of the hadron carried by the interacting parton in the infinite momentum frame. For electron scattering from a free nucleon, x ranges from 0 to 1. For scattering from a nucleus of mass number A, x ranges from 0 to $M_A/M \approx A$.

In terms of the deep-inelastic structure functions $F_1(x, Q^2)$ and $F_2(x, Q^2)$, the differential cross section for scattering of an unpolarized electron in the laboratory frame can be written as

$$\frac{d^2\sigma}{d\Omega dE'} = \frac{4\alpha^2 E'^2}{Q^4} \cos^2(\theta/2) \big[F_2(x, Q^2)/\nu \\ + 2\tan^2(\theta/2) F_1(x, Q^2)/M \big] \ , \qquad (2)$$

where α is the fine structure constant. For brevity, this doubly differential cross section is denoted by the symbol σ. When Q^2 and $\nu \to \infty$, the structure functions will only depend on the ratio Q^2/ν or equivalently on the variable x [2]. Thus, in this scaling region the structure functions are simply a function x. In the quark parton model (QPM), this scaling behavior is due to the elastic scattering from moving quarks inside the nucleon. In this model, the structure function F_2 is given by

$$F_2(x) = \sum_f e_f^2 x q_f(x) \ . \qquad (3)$$

where the distribution function $q_f(x)$ is the expectation value of the number of partons of flavor f (up, down, strange...) in the hadron, whose longitudinal momentum fraction lies within the interval $[x, x + dx]$ and e_f is the charge of the parton.

In the region of deep-inelastic scattering (DIS), the structure functions do not scale exactly, and instead depend logarithmically on Q^2. This is a consequence of QCD, in which the parton distribution functions (PDFs) are not scale independent, but evolve with Q^2. The logarithmic scaling violations associated with QCD do not break down the connection between the structure function and the underlying PDFs, but simply reflect the scale-dependence of the PDFs.

Along with the Q^2 dependence associated with QCD, additional power corrections appear at lower Q^2 values, mainly at large x. So-called "target mass corrections" [3] yield deviations from scaling at finite Q^2 values arising from terms neglected in the high-Q^2 approximations used in the ideal scaling limit. In addition, higher-twist effects, associated with breakdown of the assumption of incoherent elastic scattering from individual quarks at lower Q^2, also modify the scaling behavior. This is most clearly manifested in the appearance of clear structures in the inclusive structure function associated with production of individual resonances.

Analogous to the absorption cross section for real photons, the F_1 and F_2 structure functions can be expressed in terms of longitudinal (σ_L) and transverse (σ_T) virtual-photon cross sections

$$\frac{d^2\sigma}{d\Omega dE'} = \Gamma \left[\sigma_T \left(x, Q^2 \right) + \epsilon\, \sigma_L \left(x, Q^2 \right) \right] \ , \qquad (4)$$

where $\epsilon = \Gamma_L/\Gamma_T = \left[1 + 2 \left(1 + Q^2/4M^2 x^2 \right) \tan^2 \frac{\theta}{2} \right]^{-1}$ is the virtual polarization parameter, Γ is the virtual photon flux, and Γ_L and Γ_T defines the probability that a lepton emits a longitudinally or transversely polarized virtual photon.

The ratio of longitudinal to transverse virtual-photon absorption cross section is given by

$$R(x, Q^2) = \frac{\sigma_L}{\sigma_T} = \left[\left(1 + \frac{\nu^2}{Q^2} \right) \frac{M}{\nu} \frac{F_2(x, Q^2)}{F_1(x, Q^2)} \right] - 1 \ . \qquad (5)$$

Using equations 2 and 5, the per-nucleon cross section (cross section divided by the total nucleon number) ratios for two different nuclei A_1 and A_2 can be written as

$$\frac{\sigma_{A_1}}{\sigma_{A_2}} = \frac{F_2^{A_1} \left(1 + \epsilon R_{A_1} \right) \left(1 + R_{A_2} \right)}{F_2^{A_2} \left(1 + \epsilon R_{A_2} \right) \left(1 + R_{A_1} \right)} \ . \qquad (6)$$

Note that when $\epsilon = 1$ or $R_{A_1} = R_{A_2}$, the ratio of the F_2 structure functions is identical to the cross section ratio. In this and all previous extractions of the EMC effect, it is assumed that R is target independent, and therefore the cross section ratios correspond to the F_2 structure function ratios.

Because the structure functions depend on Q^2, the ratio may also have a Q^2 dependence which we must account for in comparing our data to measurements at other different Q^2 values. However, the effect of QCD evolution on the ratios should be essentially negligible as the evolution is nearly identical for all nuclei, and so cancels in the ratio. The main effect of the target mass corrections can be applied with a simple change of variables from Bjorken-x to Nachtmann-ξ when comparing measurements at different Q^2 (Sec. III K). Thus, in kinematics where any remaining higher-twist contributions are small or A independent, the comparison of EMC ratios from experiments at different Q^2 values is straightforward. Accounting for this change of variables mentioned above, it has been shown that the EMC ratios are independent of Q^2 down to very low values of Q^2 and W^2, well below the typically-defined DIS regime [4, 5].

B. EMC effect

Nuclei consist of protons and neutrons bound together by the strong nuclear force, with binding energies of 1–2% of the nucleon mass, and characteristic momenta below 200–300 MeV/c. Because DIS involves incoherent scattering from the quarks, and the energy and momentum scales associated with nuclear binding are small compared to the external scales in DIS, the naive assumption was that the nuclear structure function in high-energy scattering from a nucleus with Z protons and N neutrons would simply be the sum of the proton and neutron structure functions:

$$F_2^A(x, Q^2) = ZF_2^p(x, Q^2) + NF_2^n(x, Q^2) \ . \qquad (7)$$

Even before the discovery of the EMC effect, Fermi motion of the nucleons in the nucleus was known to play a role in nuclear structure functions. While the typical scale of the Fermi momentum is small compared to the momentum scale of the probe, the longitudinal component is directly added to the momentum of the virtual photon and cannot be completely neglected. It is necessary to perform a convolution of the PDFs of the proton and neutron with the momentum distribution of the nucleons in the nucleus [6]:

$$F_2^A(x) = \int_x^A dz \, f_N^A(z, \epsilon) F_2^N\left(\frac{x}{z}\right) \ , \qquad (8)$$

where the longitudinal momentum distribution function $f_N^A(z, \epsilon)$ for the nucleon is given by,

$$f_N^A(z, \epsilon) = \int d^4p \, S_N(p) \, \delta\left(z - \left(\frac{p \cdot q}{M_N q_0}\right)\right) \ . \qquad (9)$$

Here, $S_N(p)$ is the spectral function of the nucleus (assumed to be identical for protons and neutrons), z is the light-cone momentum carried by the nucleon and ϵ its removal energy. The four-momenta of the struck nucleon and virtual photon are given by p and q, where q_0 is the energy transferred by the virtual photon. One can think of the convolution as "smearing" the nucleon PDF in x, yielding little change where the PDF is relatively flat in x, and larger effects where it grows or falls rapidly. Calculations showed that the effect was minimal at low x values, but that the convolution has a large impact for $x \gtrsim 0.6$, where the PDF of the nucleon falls rapidly [7–9].

Therefore, it came as a surprise when this expectation was shown to be incorrect by measurements which showed significant effects on the nuclear PDF for nearly all values of x [1]. As part of a comprehensive study of muon scattering, the European Muon Collaboration compared data from iron with data from deuterium by forming a per-nucleon structure function ratio of these targets. Since the x distributions of up and down quarks differ, yielding different structure functions for the proton and neutron, EMC ratios are usually taken as a ratio of a heavy isoscalar target to deuterium. This cancels out the contribution due to the difference between the proton and neutron structure function but yields a ratio which depends on the nuclear effects in both the heavy nucleus and the deuteron. For non-isoscalar nuclei, a correction is typically applied to estimate the effect of the neutron excess in heavy nuclei. Note that many calculations provide the ratio of the heavy nucleus to the sum of free proton and neutron structure functions. This provides a more direct measure of the nuclear effects in the nucleus, but cannot directly be compared to the data, as the lack of a free neutron target makes direct measurements of the free neutron structure function impossible.

When plotted as a function of x, the EMC ratio shows significant deviation from unity. The deviation of this ratio from unity was unexpected, and, this A dependence in deep-inelastic scattering is known as the EMC effect. This discovery had a significant impact on views of the structure of nuclei, and has spurred discussion of the importance of the concepts of quarks, gluons and QCD to nuclear physics.

Though the boundaries are somewhat arbitrary, generally the x dependence of the cross section ratios are divided into four regions in x. The gross features of the data are; (1) the region $x < 0.1$, where the nuclear cross sections are suppressed (known as the shadowing region); (2) the region $0.1 < x < 0.3$, where the nuclear cross sections are slightly enhanced compared to nucleon cross sections (anti-shadowing region); (3) the region $0.3 < x < 0.7$, where a large suppression of the nuclear cross section is observed ("EMC effect" region), and (4) the region $x > 0.7$ where the A/D cross section ratio increases and grows beyond unity due to the convolution ("Fermi smearing") effects.

C. Previous measurements of the EMC effect

After the initial observation of an unexpected nuclear dependence in the structure functions of heavy nuclei [1], additional measurements were performed at both CERN [10–12] and SLAC [13–16]. Further measurements by the European Muon Collaboration (EMC) [17] and the New Muon Collaboration (NMC) [18, 19] significantly improved the precision and kinematic range of measurements at low x, mapping out in detail the shadowing region for a range of nuclei. The HERMES collaboration also measured DIS cross sections on several nuclear targets including ^{3}He [20, 21]. The data in the anti-shadowing region are consistent with unity, while data at higher x have large uncertainties.

Focusing on the high-x region, SLAC experiment E139 [16] mapped out the EMC effect for ^{4}He, Be, C, Al, Ca, Fe, Ag, and Au in the range $0.09 < x < 0.9$ and $2 < Q^2 < 15$ GeV^2. Examining the target ratios, and in particular their deviations from unity, the experiment showed no significant Q^2 dependence and an identical x dependence for all nuclei, although the high-x behavior of ^{4}He appeared to differ, but not in a significant fashion given its large uncertainties. The A-dependence of the nuclear effects could be parameterized several different ways: varying logarithmically with A, linearly with $A^{-1/3}$, or being proportional to the average nuclear density (assuming a uniform sphere based on the measured nuclear charge radius). Exploiting the local density approximation [22], it was found that the EMC effect scales as $A^{-1/3}$ which allowed for data from finite nuclei to be extrapolated to infinite nuclear matter [23].

The universal x dependence and weak A dependence for heavy nuclei makes it difficult to evaluate models of the EMC effect [24–26]. In addition, the EMC effect at very large x values (>0.7) had not been well measured. The typical DIS requirement, $W^2 > 4$ GeV^2, yields extremely high Q^2 measurements for $x \gtrsim 0.8$, where the cross sections are extremely small. However, an extraction of EMC ratios from JLab experiment E89008 in the resonance region ($1.2 < W^2 < 3.0$ GeV^2 with $Q^2 = 3$–4 GeV^2) demonstrated that the nuclear effects in the resonance region and DIS region are identical [4]. This implies that relaxing the constraint on W^2 may allow for measurements at larger x values than previously accessed. Precise measurements at large x allow for tests of the convolution model where other effects are expected to be small, providing a constraint on the convolution effects which must be accounted for at all x values.

D. Theoretical models

Even though it has been almost four decades since the discovery of the EMC effect and there are extensive data on its x and A dependence for $A \geq 12$, there is no clear consensus as to its origin. The EMC effect has been under intense theoretical and experimental study since the original observation (see the reviews [24–28] and references therein). The models used to explain the observed effect range from traditional nuclear descriptions in terms of pion exchange or binding energy shifts, to QCD inspired descriptions that include effects from dynamical rescaling, multi-quark clustering and deconfinement in nuclei, some of which involve changes to the nucleon's internal structure when in the dense nuclear medium.

Traditional calculations begin with the convolution model, where the nucleon motion modifies the effective x and Q^2 values of the e–N interaction, such that the virtual photon probes a modified quark distribution compared to the stationary nucleons. In general, these convolution calculations result in a suppression of the nuclear structure function at large x, but do not describe the full depletion observed in EMC effect measurements. Another drawback of the convolution calculations is that they often fail to describe the nuclear dependence of the Drell-Yan reaction observed by the Fermilab E772 collaboration [29].

Although convolution calculations can be improved with the addition of binding effects, Miller and Smith [30, 31] have demonstrated that binding alone is insufficient to reproduce the EMC effect. However, these calculations do not include off-shell effects. The calculation by Benhar et al. [32] uses nuclear wave functions that include high momentum tails in the nucleon momentum distribution while adding a model to handle the off-shell nucleon cross-section effects. The combination of these two ingredients results in a significant depletion of the structure function at large x (larger than the observed EMC effect) and the addition of contributions from "nuclear pions" is required to provide quantitative agreement with EMC measurements. Kulagin and Petti [33] also start from a convolution approach including binding effects, shadowing, and contributions from nuclear pions, yielding roughly half of the observed EMC effect. Off-shell effects are then introduced and their contribution is tuned to give good agreement with the experimental data. These calculations that predict a significant role for off-shell effects are particularly interesting in light of potential explanations for the observed correlation between the size of the EMC effect and the number of short-range correlated pairs (SRCs) in nuclei [34–36].

Frankfurt and Strikman [37, 38] account for some of the deficit in the momentum-sum rule for the nucleons by a modification to the Coulomb field of the nucleus. Starting from a convolution model which uses the separation energy, accounting for the momentum in the Coulomb field simply accounts for loss of momentum from the nucleons; it does not yield an additional suppression of the structure function at large x. However, it would suggest that proposed modifications to the nuclear pion field, used to explain the deficit of the momentum sum rule in some calculations, may be overestimated in heavy nuclei where the modification of the Coulomb field is more significant.

Additional contributions that have been examined are

virtual constituents of the nucleus which are not present in a nucleon. In the dense environment of a nucleus, one may have color-singlet clusters of 6, 9,... valence quarks [39, 40] or hidden-color configurations [41, 42]. The PDFs of these exotic objects is expected to differ significantly from the sum of individual nucleons, leading to a modification to the nuclear PDF. Estimates of such clusters predict a modest contribution to the PDFs in the EMC region, but show a larger impact that may be experimentally accessible at larger x, as such configurations contribute to the structure function well beyond $x = 1$ [24, 26, 43, 44].

Finally, some calculations invoke a modification to the internal structure of individual nucleons within the dense medium of the nucleus. Different rescaling models [45–47] have been proposed to explain the EMC effect, based on a change in the nucleon radius due to partial deconfinement in the nuclear medium. In terms of QCD, a change in confinement means a change in Q^2. Thus, QCD evolution starts at lower Q^2 for a free nucleon, and, hence, the QCD radiative processes per nucleon are larger in a bound nucleon than in a free nucleon. In this case, scaling is referred to as "dynamic" because of the evolution of the quark, anti-quark and gluon distributions. Close *et al.* [48] shows that an increase in confinement size could explain the data on a medium nucleus such as iron but fail to explain the data for $x \gtrsim 0.65$, since there is no inclusion of Fermi motion effects.

There are other models involving medium-modified nucleons that do not use a rescaling of Q^2. In such models the quark wave function of a nucleon is modified by external fields generated by the surrounding nucleons. Quark-meson coupling models [49] include the effect of the nuclear medium by allowing quarks in nucleons to interact via meson exchange and additional vector and scalar fields. These models have been applied to the study the EMC effect in unpolarized and polarized [50, 51] structure functions, as well as other observables for nuclei and nuclear matter [52]. In addition, calculations for finite nuclei [51] show a significant difference between the polarized and unpolarized EMC effect and also predict flavor dependent effects [53]. Recent work by Miller and Smith use a chiral soliton model to relate nucleon form factor modification [54], the EMC effect in polarized [55] and unpolarized [30] structure functions.

E. Physics motivation behind E03103

The experiment reported here, JLab E03103, was designed to precisely map out the x, Q^2 and A-dependence of inclusive electron scattering from light to medium heavy nuclei, with emphasis on light nuclei and the large-x region [56]. Results for the EMC ratios for the light nuclei have been reported in reference [57]. The analysis presented in this work uses an updated isoscalar correction prescription (described in Sec. III J) as well as a slightly modified radiative correction scheme (see Sec. III H) as compared to reference [57]. The impact of these modifications on the light target results is not large (at most 1% for the isoscalar correction and 0.6% for the radiative corrections), but does result in slightly different cross section ratios.

While the EMC effect has been well measured in heavy nuclei, the SLAC E139 ratios for ^{4}He have large uncertainties and there were no previous measurements on ^{3}He in the valence region. Data on light nuclei are important in understanding the microscopic origin of the EMC effect as they allow direct comparison to detailed few-body calculations with minimal nuclear structure uncertainties. Data on light nuclei can also help constrain nuclear effects in the deuteron which are critical to the extraction of the neutron structure function from measurements on the deuteron [58–62]. Light nuclei allow for better tests of the A dependence of the EMC effect, while also providing measurements of nuclei more similar to the deuteron in mass and density.

In addition, studies of short-range correlations [63–70] suggest that high-density configurations play an important role in nuclei, which could potentially yield a modification of the nucleon structure function in overlapping nucleons [24, 26, 43, 44, 71, 72]. If two-body effects have a significant contribution to the EMC effect, then the EMC effect could be different in few-body nuclei than it does in heavy nuclei, where the effects may be saturated. There were also models which predicted a very different x dependence for the EMC effect for A=3,4 [73–75], so the inclusion of light nuclei was considered important as a way to look for two-body effects as a possible source of medium modification in nucleon structure.

Beyond the focus on light nuclei, E03103 emphasized large x, where Fermi motion and binding effect dominate. Because of the lack of data in this region and the limited data for few-body nuclei, many calculations of the EMC effect are performed for nuclear matter and extrapolated to lower density when comparing to nuclear parton distributions. In such cases, the important contributions of binding and Fermi motion are not modeled in detail, making it difficult to isolate contributions beyond these more conventional effects.

While many models mentioned in the previous section have had some success, most are incomplete. They may work only in a limited x range, conflict with limitations set by other measurements, or explain the data while neglecting Fermi motion and binding. However, it is clear that the effects of binding and Fermi motion are important and contribute over the entire x region, not just at the largest x values. The large x data are particularly sensitive to these effects and to the details of nuclear structure. As such, precise high-x data for both light and heavy nuclei can help to constrain these effects.

II. EXPERIMENTAL APPARATUS

Experiment E03103 was carried out in Hall C in 2004 at the Thomas Jefferson National Accelerator Facility (JLab) [76]. The unpolarized electron beam from the Continuous Electron Beam Accelerator Facility was incident on solid, liquid and high pressure gas targets. The High Momentum Spectrometer (HMS) (a magnetic focusing spectrometer) was used to detect the scattered electrons. The nominal electron beam energy (E) was measured with the Hall C arc energy measurement [77], the scattered momentum ($E^{'}$) and angle (θ) are reconstructed from the particle trajectory in the HMS.

A. Experiment kinematics

Most of the data for the experiment were taken at 5.776 GeV beam energy with beam currents of 30–80 μA. The cryogenic targets ^{2}H, ^{3}He, ^{4}He and solid targets ^{9}B, ^{12}C, ^{63}Cu and ^{197}Au were used for EMC ratio measurements while ^{1}H was used primarily for calibration. Data on all targets were taken at $40°$ and $50°$, and the cross section ratios with respect to deuterium were extracted. At high x, the kinematics were not in the conventional DIS region ($W^2 > 4\,\mathrm{GeV}^2$), so additional data were taken for ^{12}C and ^{2}H at 8 additional kinematic settings, half at E=5.776 GeV and half at 5.01 GeV, as shown in Fig. 1.
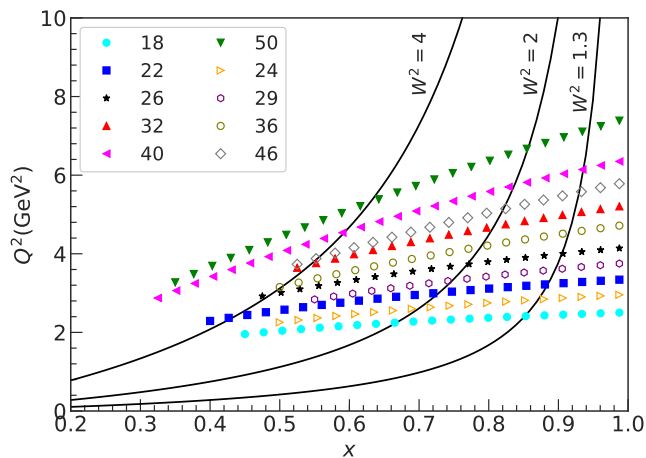

FIG. 1: (Color online) Kinematic coverage for the experiment. Contours of constant invariant mass squared are shown with black lines. Different colors represent different angles, given in the legend. Closed symbols were taken at E=5.776 GeV beam energy and open symbols at 5.01 GeV.

B. Targets

E03103 measured inclusive electron scattering from a wide range of nuclei using both cryogenic and solid tar-

gets. This experiment used the standard Hall C target ladder (see Fig. 2) which was placed inside a vertical cylindrical vacuum scattering chamber. The scattering chamber had entrance and exit openings for the beam as well as a vacuum pumping port and several view ports. The beamline was connected directly to the scattering chamber, so the beam did not pass through any solid entrance window. There were two cutouts on the chamber for the two spectrometers to detect the scattered particles, which are covered with thin (0.41 mm) aluminum windows.
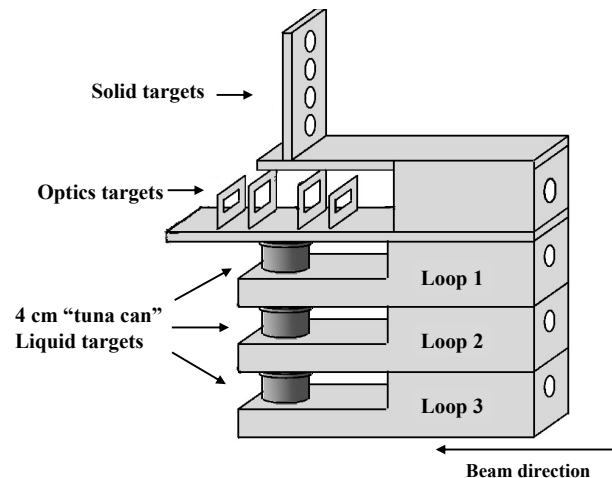

FIG. 2: A schematic side view of Hall C target ladder.

TABLE I: Nominal cryotarget dimensions. Here, $\langle t \rangle$ represents the average offset-corrected cryogen in the path of the beam and R.R.L is the relative radiation length (material thickness as a fraction of its radiation length)

Target	$\langle t \rangle$ (cm)	Density (g/cm^3)	Areal thickness (g/cm^2)	R.R.L (%)	Purity (%)
^{1}H	3.865	0.0723	0.2794(36)	0.456	99.99
^{2}H	3.860	0.167	0.6446(83)	0.526	99.95
^{3}He	3.865	0.0708	0.2736(51)	0.419	99.9
^{4}He	3.873	0.135	0.5229(85)	0.554	99.99

The target assembly contained several loops for cryogenic targets and the solid target ladder was attached above the optics sled. The target stack could be raised or lowered by an actuator in order to put the desired target in the beam path. The cryogenic targets were contained in vertical cylindrical Al cans with a diameter of ≈ 4 cm. Each loop consisted of a circulation fan, a target cell, heat exchangers and high powered heaters. The target liquid in each loop was cooled with helium gas using a heat exchanger. The liquid moved continuously through the heat exchanger, to the target cell and back. A high power heater regulated the temperature of the cryogenic targets, compensating for the power deposition by the

beam during low current or beam off periods. Solid targets were attached above the optics sled and all the foils in the solid target ladder were separated vertically.

The optics sled contained a dummy target, which consisted of two aluminum foils (aluminum alloy Al-6061-T6 - identical to the cryotarget endcaps) placed ~ 4 cm apart. These dummy targets mimicked the cell walls of the cryogenic target and facilitated the measurement of the background originating from the cell walls. The dummy targets were flat aluminum foils and were approximately 8 times thicker than the walls of liquid targets to reduce the time needed for background measurement.
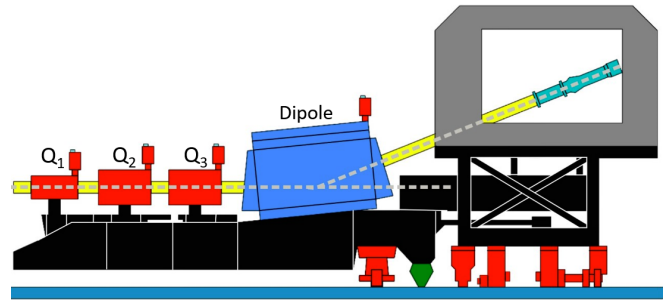

FIG. 3: (Color online) Schematic side view of the HMS. The first three magnets (red) are Q1, Q2, and Q3; the blue magnet is the Dipole. Adapted from ref. [77].

TABLE II: Solid target dimensions, relative radiation length, and purity. Here, Al(1) and Al(2) represents the aluminum foils which mimicked the cell walls of cryogenic target.

Target	Density (g/cm^3)	Areal thickness (g/cm^2)	R. R. L. (%)	Purity (%)
Be	1.848	1.8703(94)	2.87	99.0
C	2.265	0.6667(40)	1.56	99.95
Cu	8.96	0.7986(40)	6.21	99.995
Au	19.32	0.3795(38)	5.88	99.999
Al(1)	2.699	0.2626(13)	1.09	98.0
Al(2)	2.699	0.2633(13)	1.10	98.0

Areal thicknesses of the cryotargets were computed (see Table I) from the target density and the length of the cryogen in the path of the beam. Since the target cans were cylindrical, the effective target length seen by the beam differed from the diameter of the can if the beam did not intersect the geometrical center of the targets, and a correction accounting for beam offset was applied run-by-run. The target density was calculated using the knowledge of temperature and pressure.

Thicknesses of the solid targets were calculated using measurements of the mass and area of the targets. For solid targets, there is an uncertainty in the effective thickness due to uncertainty in angle of the target relative to beam direction, but this is estimated to be $< 0.01\%$. Solid targets used in the experiment and their dimensions are given in Table II. No correction is applied for the $\sim 1\%$ impurities in the ^{9}Be target, as the cross section per nucleon for ^{9}Be and heavier nuclei differs at the few percent level, so the correction is typically $\ll 0.1\%$.

C. High-Momentum Spectrometer

E03103 used the HMS to detect the scattered electrons. The HMS is a $25°$ vertical-bend spectrometer that consists of three quadrupole magnets, one dipole magnet and a detector package. The detectors are housed inside a concrete enclosure and this shield hut, along with the HMS magnets, are mounted on a steel carriage which can be rotated on a pair of concentric rails to the desired scattering angle. An octagonal collimator is placed before the entrance to the first magnet which is used to define the acceptance for a short target for particles within approximately 10% of the central momentum setting. A schematic side view of the HMS is shown in Figure 3. All magnets in the HMS are superconducting and are cooled with 4K liquid helium. The focusing properties and acceptance of the HMS are determined by the quadrupole magnets, and the central momentum is determined by the dipole. The spectrometer volume is under vacuum with thin (0.5 mm) mylar-kevlar windows at the entrance (before the collimator) and exit (after the dipole, in the detector hut). See Ref. [77, 78] for more details on the spectrometer and detector package.

There are two drift chambers in the HMS located at the front of the detector stack [79]. The drift chambers are used to find the position and trajectory of the particle at the focal plane, which are used to reconstruct the position and momentum of the scattered particle at the interaction vertex. Two sets of $x - y$ scintillators hodoscopes were used for triggering and time-of-flight measurements [77]. The detector stack also contains a threshold gas Čerenkov counter used for electron identification [77]. The HMS Čerenkov detector is a large cylindrical tank (inner diameter ≈ 150 cm and length ≈ 165 cm). It has two front reflecting mirrors which focus the light onto two PMTs. The circular ends of the tank are covered with 0.1 cm aluminum windows. For E03103, the detector was filled with 5.15 psi (~ 0.35 atmospheres) of Perfluorobutane (C_4F_{10}) at room temperature. At this pressure and temperature, the index of refraction of the gas is 1.00050, yielding a threshold momentum of 16 MeV for electrons and 4.4 GeV for pions. The pion threshold was above the momentum range of E03103 except for the lowest angles, where the π/e ratio is small and the separation between electrons and pions in the calorimeter is sufficient to yield a negligible pion background.

A lead glass calorimeter detector [80] was used in conjunction with the Čerenkov detector for electron identification. The HMS calorimeter consists of 10 cm×10 cm×70 cm blocks of TF-1 lead glass, positioned at the

rear of the detector hut. The blocks are arranged in four layers with 13 blocks per layer for a total thickness of 14.6 radiation lengths along the particle direction. The calorimeter blocks are calibrated by using the gas Čerenkov detector to identify a clean sample of electrons, and the scale factor applied ADC signals from the individual blocks are adjusted to provide a spectrum peaked at the electron momentum as determined from the tracking. Thus, Electrons (or positrons) entering the calorimeter deposit their entire energy and the normalized energy spectrum, $E_{\rm cal}/E'$, is peaked around 1. Pions typically deposit ~ 300 MeV in the calorimeter and the $E_{\rm cal}/E'$ distribution peaks around 0.3 GeV/E'.

III. DATA ANALYSIS

The data acquisition system used for E03103 was the CODA (CEBAF Online Data Acquisition) software package. CODA events from the individual run files were decoded by the standard Hall C replay software (ENGINE). It reads the raw data written by the data acquisition system, decodes the detector hits, locates possible tracks and particle identification information for each event, and calculates different physics variables. Input and output of the ENGINE are handled using the CEBAF Test Package (CTP). ENGINE makes use of CERN HBOOK libraries and provides output as ASCII report files (scalers, integrated charge ...), histogram files (ADC/TDC spectra for different detectors) and the reconstructed event-by-event data as ntuples. Detailed cuts, corrections and other analysis details will be discussed in the following sections.

A. Methodology of Cross Section Extraction

The measured inclusive electron scattering cross section at scattered electron energy E' and a central angle θ_c was extracted using a simulation of the electron scattering process via the ratio method,

$$\sigma_{\rm data}^{\rm Born}(E',\theta_c) = \frac{Y_{\rm data}}{Y_{\rm sim}}\,\sigma_{\rm model}^{\rm Born}(E',\theta_c) \qquad (10)$$

where $\sigma_{\rm data}^{\rm Born}(E',\theta_c)$ denotes the differential cross section $\frac{d^2\sigma(E',\theta_c)}{dE'd\Omega}$, $Y_{\rm sim}$ represents the simulated yield which includes the features of the detector acceptance and the model radiated cross section, $Y_{\rm data}$ is the charge normalized yield integrated over the acceptance of the experiment and $\sigma_{\rm model}^{\rm Born}(E',\theta_c)$ represents the Born model cross section. To the extent that the simulation properly includes the corrections, efficiencies, and acceptance, the ratio of experimental to simulated yield will simply reflect the error in the initial cross section model.

$Y_{\rm data}$ is the number of detected electrons, averaged over the kinematics, divided by the efficiency- and deadtime-corrected luminosity of the measurement, so that $Y_{\rm data}$

represents the normalized yield for an ideal detector averaged over the acceptance of the experiment. The calculation of $Y_{\rm sim}$ must result in the same acceptance-averaged normalized yield, and so must include a detailed model of the acceptance as well as all of the physics effects required to go from the starting Born cross section model to the final observed counts, i.e. radiative effects, multiple scattering, energy loss, etc.... In addition, because this is the integrated yield over the acceptance, the cross section model must do a reasonable job of accounting for the cross section variation across the acceptance. Note that the *position-dependent* inefficiencies are applied to the simulation, rather than the data, as discussed in Sec. III B 4. Energy loss is included event-by-event in the simulation, to yield a realistic distribution. A single correction for the median energy loss was applied to both data and simulation to remove the average kinematic offsets.

1. Extraction of experimental yield

Each kinematic setting contains data taken over one or more runs. Each run is analyzed separately, with detector and acceptance cuts applied and the efficiency and other experimental correction factors calculated run-by-run. The efficiency-corrected and charge-normalized yield for all the runs in a given setting, with

$$Y_{\rm data}^{\rm tot} = \frac{\sum_i N(i)}{N_{\rm sc}\ \sum_i C_{\rm data}(i)\,Q_{\rm tot}(i)}, \qquad (11)$$

where N_i is the total number of events that passed all cuts for the ith run in the given setting, $Q_{\rm tot}(i)$ is the total accumulated charge and $N_{\rm sc}$ is the number of scattering centers in the target; $N_{\rm sc} = \rho t N_A/M$ where ρ is the density, t is the thickness, M is the atomic mass of the target and N_A is Avogadro's number. The factor $C_{\rm data}(i)$ in Eq. 11 is the correction factor which includes experimental efficiencies and live times (fraction of time that the DAQ and computer readout systems are active); $C_{\rm data} = PS/(\varepsilon_{\rm trig}\times\varepsilon_{\rm track}\times\varepsilon_{\rm det}\times t_{\rm comp}\times t_{\rm elec})$ where PS is the prescale factor used to control the trigger rate when the data is taken, $\varepsilon_{\rm trig}$ corrects for the events lost due to inefficiency at the trigger level, $\varepsilon_{\rm track}$ is the tracking efficiency, $\varepsilon_{\rm det}$ denotes the global detector efficiencies, and $t_{\rm comp}$ and $t_{\rm elec}$ are the computer and electronic live time, respectively.

Because we are only interested in primary beam electrons which scatter in the target, we have to subtract the contribution of electrons which scatter in the target entrance and exit windows (for the cryogenic targets) and secondary electrons which come from other processes. The subtraction of the cryotarget endcap contribution is discussed in Sec. III C 1, and the secondary electrons in Sec. III C 2.

2. *Extraction of simulated yield*

In order to evaluate $Y_{\rm sim}$ one needs to account for the finite acceptance of the HMS using a detailed model of the spectrometer acceptance. Cuts are applied to the measured and simulated distributions to limit the data to events where the momentum acceptance is well understood. These cuts, given in Table III are large enough in angle so that the collimator defines the angular acceptance, but are effective in removing in-scattering events. These are electrons that are outside of the nominal acceptance but which reach the detectors because of scattering from an aperture in the spectrometer. Because of the scattering inside the spectrometer, these events tend to reconstruct to trajectories outside of the acceptance and are thus removed by the acceptance cuts.

TABLE III: Acceptance cuts used in the analysis for data and simulation. Here, δ is the relative deviation from the central momentum and $x'_{\rm tar}$ and $y'_{\rm tar}$ are the out-of-plane and in-plane angles of the reconstructed tracks at the target.

Variable	cut value
abs(δ)	< 9%
abs($x'_{\rm tar}$)	< 120 mr
abs($y'_{\rm tar}$)	< 40 mr

The Hall C single arm Monte Carlo is used to extract the simulated yield. Each event is randomly generated in the target coordinates (x, y, z), while the quantities $\delta, y'_{\rm tar}, x'_{\rm tar}$ are randomly chosen within their allowed limits. Then the particles are projected forward and transported to the detector hut using transport matrix elements calculated by the COSY INFINITY program [81], which models magnetic transport properties of the spectrometer. Events that fail to pass through the different apertures defined in the Monte Carlo are rejected. Multiple scattering is simulated as the electrons pass through material in the spectrometer, and so the simulation is run for each spectrometer momentum setting to account for the energy-dependence of the scattering. If the particle successfully traverses the spectrometer and passes all the criteria in the detector then it is accepted.

After applying cuts and binning the Monte Carlo counts in the same manner as data, the simulated yield is given by,

$$Y_{\rm sim} = \mathcal{L} \sum_{events} \varepsilon'_{\rm det} \left(\frac{d\sigma}{d\Omega dE'} \right)^{\rm rad}_{\rm model}$$
$$\times J(\Omega \to x'_{\rm tar} y'_{\rm tar}) \Delta E' \Delta x'_{\rm tar} \Delta y'_{\rm tar} \quad (12)$$

where $\mathcal{L}$ is the Monte Carlo luminosity, $\varepsilon'_{\rm det}$ accounts for any position-dependent efficiencies in the detectors, and $\left(\frac{d\sigma}{d\Omega dE'}\right)^{\rm rad}_{\rm model}$ is the cross section model (including radiative effects). $J(\Omega \to x'_{\rm tar} y'_{\rm tar})$ is the Jacobian that transforms between the spherical solid angle ($d\Omega$) and the spectrometer angles, x', and y', which is required since the Monte Carlo event generation is performed in spectrometer coordinates. In this analysis 5×10^6 events were generated for each kinematic setting with generation limits $\delta = \pm 15\%$, $x'_{\rm tar} = \pm 100$ mr and $y'_{\rm tar} = \pm 50$ mr. Once the measured and simulated yields have been obtained, their ratio is applied as a correction factor to the initial Born cross section used in the simulation to extract the final cross sections (Eq. 10).

B. Efficiencies

In the cross section analysis, we apply particle identification (PID) cuts on the signals from the gas Čerenkov counter and lead-glass calorimeter to distinguish electrons from other negatively charged particles. Because of this, we must also correct for losses of real electron events when these cuts are applied arising from detector-related inefficiencies. There are additional losses due to trigger and tracking related inefficiencies.

1. *Trigger efficiency*

The trigger was designed to be efficient for electrons while suppressing other particle types. The electron trigger is described in detail elsewhere [77, 82, 83], and the key points are summarized here. There are two main electron triggers. The first (ELHI) requires signals from 3/4 hodoscope layers, and both preshower and total calorimeter energy exceeding fixed thresholds. The second (ELLO) requires a Čerenkov signal and two out of three of the following: 3/4 hodoscope planes, 2/4 planes (one from the front and one from the back), or a calorimeter signal exceeding a threshold that is lower than used for ELHI. The final electron trigger is the combination of ELLO and ELHI signals. This trigger provides modest pion rejection while being relatively insensitive to possible lower efficiency in a particular component of the trigger, i.e., the Čerenkov, calorimeter, or hodoscopes.

Because there were no problems with the operation of the detectors, the final trigger level efficiency was extremely high. The efficiency for a good event to give a signal for ELHI was determined run-by-run, and found to be 99.2% on average, while the efficiency for ELLO was 99.7%. Although ELLO required both a signal from the calorimeter and Čerenkov detectors, ELHI required only one PID signal, making the trigger efficiency high even if one of the detectors had a low efficiency. Accounting for all of these effects, the trigger efficiency is 99.7% [83], and was largely rate and kinematic independent, yielding a negligible uncertainty in the cross section ratios.

2. Tracking efficiency

The normalized yields are also corrected for tracking inefficiency. In some cases, real events do not yield a good track because of noise, hardware inefficiency, or imperfections in the tracking algorithm. In other cases, events are recorded for which there is not a good electron track going through the drift chambers, in which case the lack of a track does not represent an inefficiency. A series of cuts are applied to identify events for which an electron passed through the drift chambers and should have yielded a good track. The fraction of those events which fail to give a track is taken to be the tracking inefficiency.

First, we select electrons by requiring that the event yielded a large signal in the Čerenkov and calorimeter detectors. We exclude events which hit scintillator paddles near the edges of each plane, to suppress events which may have missed the chamber but still hit the hodoscope and generated a trigger. Finally, we exclude events with more than 25 hits per chamber, as previous studies indicate that these come from electrons hitting apertures near the entrance of the detector, yielding a shower of particles. Because they hit an aperture near the entrance, they are not within the nominal acceptance of the detector and should not be treated as good tracks that were lost.

This tracking efficiency correction was applied on a run-by-run basis. At low rates, the inefficiency was approximately 2%, with a small reduction at high rates (up to 4% total inefficiency) which is consistent with the expected loss due to rejection of events with real multiple tracks. When there are two real tracks in the event, only one trigger is registered and read out, so one track is corrected for in the deadtime corrections, and the other is treated as a tracking inefficiency.

3. Calorimeter cut efficiency

To reject pions, we require that the energy deposited in the calorimeter be at least 70% of the reconstructed momentum ($E_{cal}/E' > 0.7$). It is important to know how many otherwise valid events are lost when we place a cut on the calorimeter distribution. To determine the fraction of electrons lost due to the calorimeter cut, we need to identify a clean and unbiased sample of electrons. For this analysis, we used elastic scattering data, where the initial fraction of pions is small, and then apply a cut on the Čerenkov detector to yield a pure electron sample. While elastically scattered electrons tend to populate a limited region in the acceptance of the spectrometer, this region can be moved across the acceptance by changing either the angle or central momentum of the spectrometer, allowing us to map out the response of the spectrometer throughout the acceptance. We use these scans to verify that the cut efficiency is uniform across the acceptance. The efficiency is found to be constant for E' above 1.7 GeV (99.89%), but below this momentum, the efficiency starts to decrease mainly due to decreasing resolution of the calorimeter. This falloff is approximately linear, dropping the efficiency by 0.3% for $E' \approx 0.7$ GeV/c [83] and is parameterized as a function of the scattered electron momentum and is used to correct data in the analysis. The efficiency measured with elastics is consistent with the efficiency extracted using inelastic kinematics which populate the full acceptance, where the kinematics have few enough pions for the Čerenkov to yield a pure electron sample.

4. Čerenkov cut efficiency

Another cut was applied on the number of photo-electrons collected by the Čerenkov detector in order to distinguish electrons from pions. In addition to the pion-rejection cut in the calorimeter, we also require the Čerenkov detector sees at least 1.5 photo-electrons. To measure the electron efficiency of this cut, we identify a pure sample of electrons using elastic scattering kinematics along with a cut on the calorimeter.

During the analysis it was found that the signal from the Čerenkov detector was lower near the vertical center of the detectors, corresponding to $\delta = 0$. This is due to the gap between the upper and lower mirrors. In addition to this δ-dependent inefficiency, the Čerenkov has a momentum-dependent inefficiency that was parameterized in terms of both δ and the HMS momentum setting. The efficiency is close to 100% for momenta above the spectrometer central momentum ($\delta > 0.5\%$), 1–2% lower on the low-momentum side of the acceptance, with loss of up to 2–4% efficiency in the central $\pm 0.5\%$ of the momentum acceptance (the inefficiencies are larger at low momentum settings). For details, see Ref. [83].

C. Backgrounds

In addition to the scattered electrons, there are secondary electrons that are in the acceptance of the detector due to other physical processes which constitute a background for the measurement. This background mainly consists of scattered electrons from the cryotarget cell wall, pions that survive the nominal PID cuts and are treated as scattered electrons, and secondary electrons from pair production after bremsstrahlung in the target or π^0 which decay to photons. The following subsections discuss each of these processes, and how we estimate and correct for them in the analysis.

1. Background from target cell wall

Since the cryogenic targets were contained in aluminum cells, electrons scattered from the cell walls also contribute to the total number of detected events. This contribution is measured and subtracted from the total

detected events. The cryocells were made of Al 7075 which has a density of 2.7952 g/cm^3 and the thickness of the cell walls was ~0.12 mm. The electrons traverse two cell walls, and since the cryotarget thickness varies between 0.2 to 0.6 g/cm^2, the typical size of the background contribution is between 10% to 20%. We used a dummy aluminum target to directly measure the cell wall contribution to the total yield. The dummy target consists of two Al foils (Al 6061- T6) separated by ~4 cm which are ~8 times thicker than the cryocell walls, thus allowing a higher luminosity and a smaller data acquisition time. During the experiment dummy data were taken at the same kinematics as the cryotarget data. Dummy data are treated in the same way as cryotarget data and the normalized dummy yield is subtracted from the cryotarget yield. Thus the total yield is

$$Y = Y_{\text{cryo}} - \left[\frac{R_{\text{dummy}}^{\text{ext}}}{R_{\text{walls}}^{\text{ext}}} \frac{T_{\text{walls}}}{T_{\text{dummy}}} \right] \times Y_{\text{dummy}}, \qquad (13)$$

where T_{walls} and T_{dummy} are the thicknesses of the cell walls and the dummy respectively, Y_{cryo} and Y_{dummy} are the measured cryotarget yield and dummy yield respectively, and the ratio of $R_{\text{dummy}}^{\text{ext}}$ and $R_{\text{walls}}^{\text{ext}}$ represents a correction factor which is applied to account for differences in radiative effects between the dummy target and the cryotarget cell walls. The correction was found to be about 5% for larger scattering angles at low x values and smaller for other angles.

2. Charge symmetric background (CSB)

Most of the electrons observed in the spectrometer are beam electrons that scattered in the target. However, the incident electron can also interact with the target nuclei and produce neutral pions in the target. These pions can decay into high energy photons which produce an equal number of positrons and electrons and these electrons can be detected in the HMS and treated as scattered electrons. This contribution is generally small, but it can be a significant at kinematics corresponding to scattering at low x and high Q^2.

The total number of electrons detected in the spectrometer is $e_{\text{detected}}^- = e_{\text{primary}}^- + e_{\text{background}}^-$. Since an equal number of positrons and electrons are produced, the yield is charge symmetric. This allows us to estimate the number of secondary background electrons by running the spectrometer with positive polarity and detecting the positrons. During E03103, we used the HMS to take positron data for each target at all kinematic settings where the CSB was significant (the 40 and 50 degree settings at 5.78 GeV and the 46 degree setting at 5.01 GeV) allowing for a direct subtraction of the background by assuming $e_{\text{background}}^- = e_{\text{detected}}^+$. Luminosity normalized yields are used to subtract the CSB, with identical cuts applied to the positron and electron data. $R_{\text{CSB}} = \frac{Y_{e^+}}{Y_{e^-}}$ is the fraction of the detected electrons as-

sociated with CSB, and is shown in Fig. 4 as a function of x for the 50 and 40 degree data. Note that our final EMC ratios are formed from the 40 degree data, and so the correction is below 10% except for the smallest values of x and the high-Z targets.
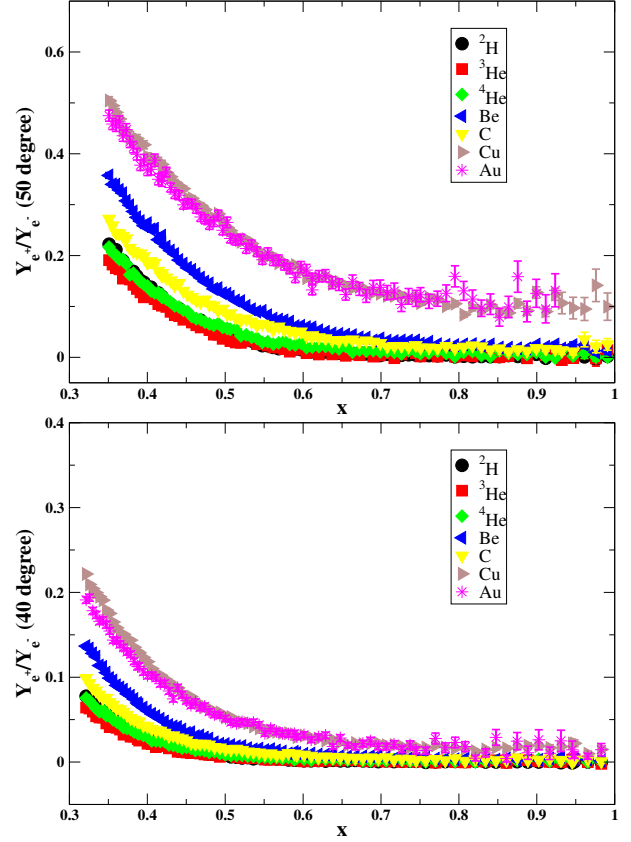

FIG. 4: The charge symmetric background as a function of x for data taken at 50 degrees (top) and 40 degrees (bottom).

3. Pion backgrounds

Pion rejection factors for the Čerenkov and calorimeter detectors are always greater than 500:1 and 100:1, respectively. Nonetheless, for runs with a high π/e ratio, there could still be a small contamination of pions after the PID cuts.

To estimate the pion background, we generate calorimeter spectra first for a data sample using electron PID cuts and then for a sample that is almost entirely pions. The pion spectrum at low E_{cal}/E' is renormalized to match the electron spectrum in that region. The pion contamination is then determined from the number of (renormalized) counts in the pion spectrum in the region $E_{cal}/E' > 0.7$ (our nominal calorimeter electron cut). This technique is illustrated in Fig. 5.

It was found that the final pion contamination is always below 0.5%. This is further suppressed as the sub-

traction of the positive-polarity data intended to remove charge-symmetric backgrounds (see section III C 2) will have a nearly identical contribution from positive pions. We estimate that any residual pion contamination is extremely small, and so we do not apply any correction, but assign a 0.2% point-to-point uncertainty to allow for a small net contribution of pions.
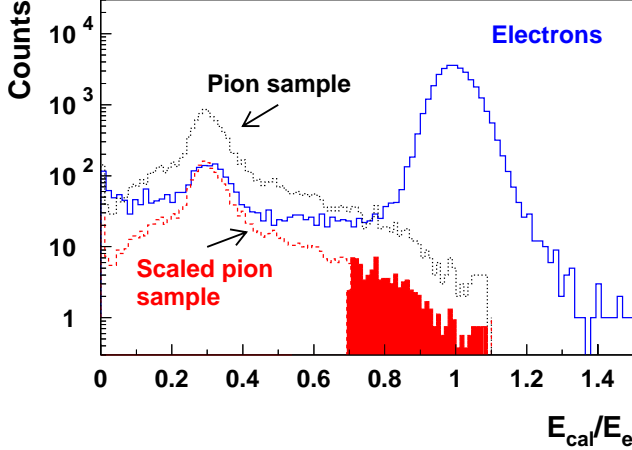

FIG. 5: (Color online) Illustration of the extraction of pion contamination using calorimeter spectra. A pion data sample (black dotted curve) is renormalized to the number of counts in an electron data sample (blue solid curve) at low E_{cal}/E'. The resulting spectrum (red dashed curve) is then used to estimate the pion contamination in the region $E_{cal}/E' > 0.7$ (solid red).

D. Target boiling corrections

When the electron beam passes through the target material of cryogenic targets, it deposits energy in the form of heat. This causes local density fluctuations, "target boiling", along the path of the beam. The boiling effects depend on the beam current, beam raster size and the thermal properties of targets. We perform luminosity scans, measurements of the yield at fixed kinematics with varying beam currents, to estimate the boiling effects. In addition to measuring the effect on the cryogenic targets, we also take data on carbon as a reference measurement, to ensure that corrections for rate-dependent effects do not introduce variations which are misinterpreted as density fluctuations.

A small current dependence was observed for the carbon target, even after correcting for all known rate-dependent effects. Because the beam-current monitors have an uncertainty in their DC offset, an error in that offset will produce an error in the charge that goes like the inverse of the beam current. The effect in carbon was small enough to be consistent with the uncertainty in the BCM offset uncertainty, and so a correction to the BCM offset was inferred from the current dependence of the carbon yield. The hydrogen and deuterium targets did not show any residual slope after correcting for the BCM offset, but the helium targets show a linear reduction in the yield. For ^{3}He, the measured density loss was $(-3.10 \pm 0.64)\%$ at $100\,\mu A$ and for ^{4}He, $(-1.27 \pm 0.50)\%$ at $100\,\mu A$. The yield for each run is divided by a correction factor which depends linearly on the average current (excluding periods with no beam).

E. Computer and electronics deadtime

Events are also lost due to the finite time it takes to either form a trigger for an event or read out the data. During the time the trigger or DAQ systems are busy, no new events can be taken. The dead time induced by the trigger electronics is monitored on a run-by-run basis by looking at the number of events generated with final trigger module gate widths of 50, 100, 150 and 200 ns. The electronic deadtime scales with the trigger rate and nominal gate width except for the 50 ns measurement, which has an effective latency time of 60 ns. While the typical gate widths are 40 ns, the coincidences formed between different hodoscope planes have variable widths, typically 50-60 ns, so our final trigger module is set to 60 ns to minimize the event-to-event variation of the effective latency time. We calculate and apply a deadtime correction of 60 ns time the raw pretrigger rate, giving a maximum correction of 1.5% with typical values well below 0.5%.

Computer deadtime occurs when the DAQ computers are busy processing events (either digitizing fastbus information or sending the data to the DAQ computers), and are not available for processing new events. Because the events are buffered in the fastbus and VME modules, there is not a fixed latency period for each event, so we make a direct measurement of the computer deadtime and apply the correction on a run-by-run basis. We take the number of events recorded to disk divided by the number of generated triggers which should have been read out and take the ratio to be the live time. The deadtime was kept below 20% by adjusting the prescale factors, although previous tests have shown reliable operation and corrections for deadtimes well over 90% [77].

F. Cross Section Model

A cross section model is required for the bin centering corrections as well as modeling radiative effects and Coulomb distortion. The Born cross section model (known as the XEM model) is broken down into contributions from inelastic and quasielastic scattering:

$$\sigma_{\mathrm{Born}} = \sigma_{\mathrm{inel}} + \sigma_{\mathrm{qe}} . \tag{14}$$

For the quasi-elastic contribution σ_{qe}, we use a y-scaling model [84]. The scaling variable y can be interpreted as the minimum momentum of the struck nucleon

in the direction of the virtual photon. The scaling function, $F(y)$, is an energy and momentum integral of the spectral function and is defined as the ratio of the measured nuclear cross section to the off-shell cross section for a nucleon, multiplied by a kinematic factor [64, 84]:

$$F(y) = \frac{d\sigma}{d\Omega d\nu} \frac{1}{Z\sigma_p + N\sigma_N} \frac{q}{\sqrt{M^2 + (y+q)^2}}, \quad (15)$$

where Z is the number of protons in the nucleus, N is the number of neutrons, q is the three-momentum transfer, and M is the proton mass. $F(y)$ is expected to scale in y on the low energy loss side of the quasielastic peak where inelastic contributions and final state interactions are minimal. The scaling function used for ^{2}H is:

$$F(y) = (f_0 - B)\frac{\alpha^2 e^{-(ay)^2}}{\alpha^2 + y^2} + B e^{-b|y|}. \quad (16)$$

For heavier targets the high-momentum components is modified and we take:

$$F(y) = (f_0 - B)\frac{\alpha^2 e^{-(ay)^2}}{\alpha^2 + y^2} + B e^{-(by)^2}, \quad (17)$$

where the parameters a, b, f_0, B and α are fit to the $F(y)$, extracted from the data for each target. The model parameters were varied to reproduce the data from this measurement, along with the measurements covering $x \gtrsim 1$ on the same targets from Refs. [44, 69]. The model was also compared to low Q^2 quasielastic data, taken from Ref. [85]. This is important because a reliable model in this region is needed when applying radiative corrections, as events from low Q^2 quasielastic scattering, which has a large cross section, can radiate photons and contribute to higher Q^2, lower x distributions.

$F(y)$ was extracted from the data in the QE region, taken as part of E03103 and E02019 [44, 69] after subtracting the model inelastic contribution (everything except the QE contribution) [86]. After fitting $F(y)$, the updated model was used as the input for the cross section extraction, and the process was repeated until good agreement between data and the model was achieved for all settings. A small additional correction was added to improve the agreement to the QE data at large x values [86].

The inelastic contribution to the cross section is evaluated separately and added to the quasielastic contribution. For the deuteron, parameterizations of the proton and neutron structure functions (developed by P. Bosted and E. Christy [87]) are used for the full x range. They are smeared using the momentum distribution based on the fit to our QE peak [86].

For heavier nuclei, the inelastic cross section is computed somewhat differently. As for the deuteron, the model cross section is the sum of the proton and neutron structure functions smeared by the momentum distribution based on the fit to the QE peak for the nucleus [86]. In addition, for $x < 0.8$, this inelastic model is then multiplied by a target-dependent polynomial function to improve the agreement between data and model (this is required since a pure-smearing calculation will not reproduce the size or shape of the nuclear EMC effect correctly). This is smoothly joined to the full smearing prescription (with no correction) for $x > 0.9$, using an x-weighted average for $0.8 < x < 0.9$. An additional polynomial correction is applied to both the deuteron and the heavier targets to slightly suppress the inelastic cross section at large x above the QE peak [86].

The smearing calculation described above, when performed in combination with our full radiative corrections procedure is quite time consuming. Therefore, the full radiative correction was only calculated at the central spectrometer angle for a given setting. Since a radiated model is also required to describe the variation of the cross section across the spectrometer acceptance, a simplified, approximate form of the radiative correction was used in combination with the smearing calculation when calculating the two-dimensional grid in E' and θ used for Monte-Carlo weighting. An additional ad-hoc correction (a polynomial in x) was applied to this latter calculation, to compensate for the approximate form of the radiative corrections used. The data as well as the model cross sections, including the relative contributions from the inelastic piece and the quasielastic piece for ^{2}H and ^{197}Au are shown in Fig. 6.

At low Q^2 values, the quasi-elastic peak accounts for a significant portion of the total cross section at large x. The low-Q^2 QE cross section also has a large impact on the radiated model at low x and high Q^2. We have done extensive studies and compared our model with the data available from the quasielastic electron nucleus scattering archive [85]. For heavy nuclei, our model cross section was compared with world QE data down to $Q^2 = 0.5$ GeV^2, and the agreement between data and model was found to be at the 10% level near the quasielastic peak, as shown in Fig 7.

G. Other corrections

The XEM cross section model is in the Born or one-photon exchange approximation. However, higher order processes in α also contribute to the measured cross sections [88, 89] and must be applied to the starting model. To compare to the measured cross sections, all significant contributions from higher order processes must be estimated and corrected for in the measured cross section. These include traditional radiative effects, as well as the Coulomb distortion associated with the long-range interaction of the electron with the charge of the nucleus.

H. Radiative corrections

Radiative corrections need to be applied to account for higher order QED processes, the most significant of
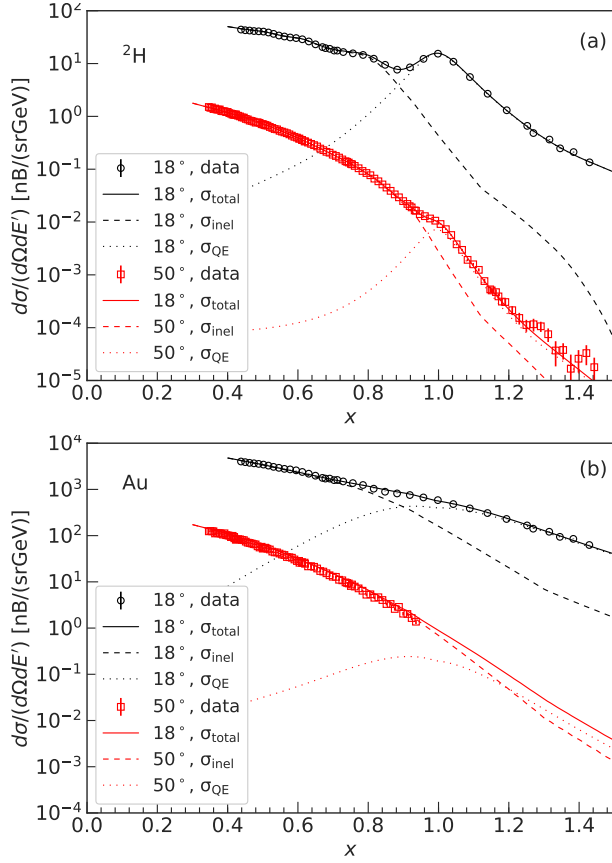
FIG. 6: (Color online) Data and model cross section for ^{2}H and ^{197}Au at selected kinematics. Here, the circles show 18 degree data and the squares show 50 degree data. Relative contribution from inelastic (dashed line) and quasielastic (dotted line) to the total cross section (solid line) are also shown in the figure.
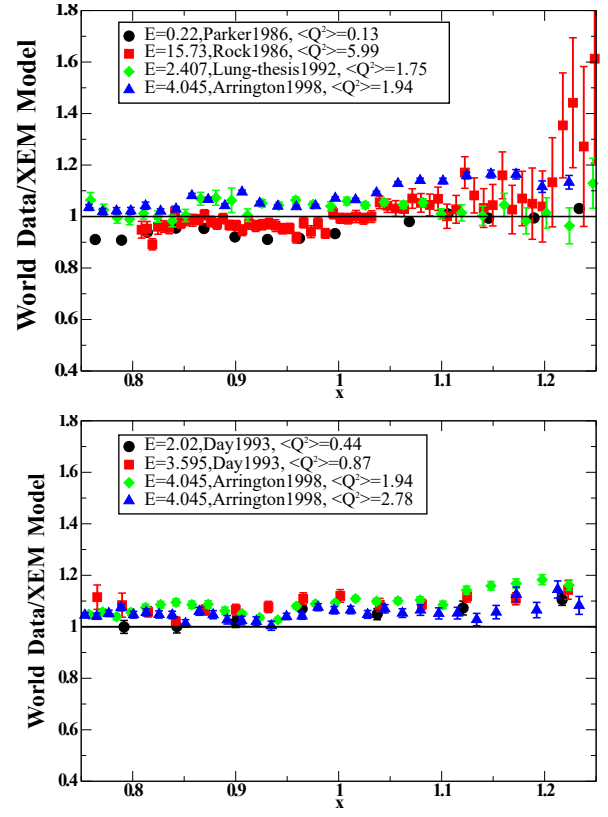

FIG. 7: (Color online) Comparison of world data from the quasielastic electron nucleus scattering archive [85] and our cross section model for a variety Q^2 settings (quoted Q^2 value corresponds to $x = 1$) for the ^{2}H (top) and ^{197}Au (bottom) targets. The shape of the QE peak is well reproduced for both targets at both low and high Q^2, yielding a nearly flat ratio of data/model over the entire x range.

which are the emission of one or more real photons by the incoming or outgoing electron or the struck quark (in the DIS regime), exchange of a virtual photon between the incoming and outgoing electron, and the fluctuation of the exchange photon into a lepton-antilepton pair. Because the elastic and quasielastic cross sections are very large at low Q^2, one must also account for low-Q^2 interactions which, due to radiation of a hard photon, end up at low x and high Q^2 values. Thus, we express the total measured radiated cross section as:

$$\sigma_{\text{meas}} = \sigma_{\text{inelastic}}^{\text{rad}} + \sigma_{\text{quasielastic}}^{\text{rad}} + \sigma_{\text{elastic}}^{\text{rad}} . \qquad (18)$$

Since the radiative tails from the QE and elastic processes are small, ($<20\%$), as are the contributions from large x, low Q^2 inelastic processes, we used the multiplicative radiative correction method. For the kinematics of this analysis, our studies indicate that the nuclear elastic tail contributes less than 0.1% to the total cross section for ^{2}H, and significantly smaller contributions for heavy nuclei, and so are neglected in the analysis.

The program used to compute the radiative effects for this analysis was developed at SLAC and is described in detail in [90]. For E03103, the external corrections are computed using a complete calculation of Mo-Tsai [88] with a few approximations. Note that, in particular, the energy-peaking approximation is not used for the computation of external contributions. This approach, "MTEQUI", uses the equivalent radiator approximation [90]. In the equivalent radiator method, the effect of "internal" Bremsstrahlung is calculated using two hypothetical radiators of equal radiation length, one placed before and one after the scattering. The internal contribution in "MTEQUI" method is evaluated by setting the radiation length of the material before and after the scattering point to zero, and ignoring the target length integral. Then the radiated model cross section is given by the sum of the internal and external contributions.

Our simulations are performed using the radiated model,

$$\sigma_{\text{rad}}^{\text{model}} = \text{external} \otimes \text{internal} \otimes \sigma_{\text{Born}}^{\text{model}}, \qquad (19)$$

The convolution involves integrating over the "internal" and "external" bremsstrahlung photon momenta and angles, and the target dimensions. To obtain $\sigma_{\rm rad}^{\rm model}$, one needs to know the cross sections over the entire kinematic range (from elastic threshold up to the kinematic point being calculated, see Figure C.1 in reference [90]). The effect of radiative correction on measured cross sections varied from a few percent to about 40%, depending on the kinematics and targets. Because the structure functions of nuclei are very similar, the internal radiative corrections and some of the external corrections cancel, yielding smaller corrections in the target ratios which depend mainly on the difference in the targets' radiation length, as shown in Fig. 8.
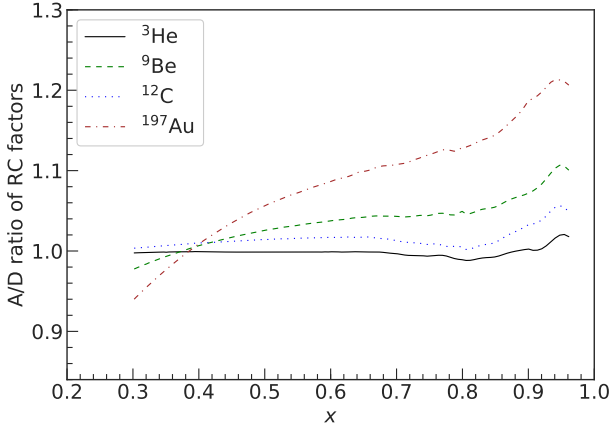
FIG. 8: (Color online) Radiative correction factor to the A/D cross section ratios for a range of targets at 40 degrees; the correction at 50 degrees is nearly identical.

I.   Coulomb corrections

The incoming electron will interact with the Coulomb field of the nucleus prior to interacting with the nucleus. Classically, once the electron enters the electron cloud of the atom, the screening of the nuclear potential is no longer perfect, and the electron will be accelerated towards the nucleus, increasing its momentum at the interaction vertex. After the scattering, there will be a similar interaction as the electron leaves the nucleus. This change in the kinematics can have a significant effect on the measured cross sections if either the Coulomb potential is large compared to the energy of the initial or final electron, or when the cross section varies rapidly with the kinematics. In addition to the modification of the scattering kinematics there is also a 'focusing' of the incoming electron plane wave which also impacts the scattering cross section. For the present analysis, we account for these effects using the improved version of the Effective Momentum Approximation (EMA) [91], following the approach given in Ref. [86].

The charge of the nucleus has two effects on the electron wave function. The initial and final state electron momenta ($\vec{k}_{i,f}$) are modified in the vicinity of the nucleus due to the attractive electrostatic potential. Secondly, the attractive potential leads to focusing of the electron wave function in the interaction region. The distorted electron wave can be approximated by [91, 92],

$$\psi_{\vec{k}_{i,f}} = \frac{|(\vec{k}_{i,f})_{\rm eff}|}{|\vec{k}_{i,f}|}\,\psi_{(0)}\,\exp\left(i\,\vec{k}_{i,f}\cdot\vec{r}\right), \qquad (20)$$

where $\psi_{(0)}$ is the Dirac-spinor with $|(\vec{k}_{i,f})_{\rm eff}| = |(\vec{k}_{i,f})| - \overline{V}$, and $\overline{V}$ is the average electrostatic potential of the nucleus.

Treating the nucleus as a spherical charge distribution, radius R_0, central potential is given by:

$$V_{(0)} = -\frac{3\alpha(Z-1)}{2R_0}\ . \qquad (21)$$

Because the standard convention is to neglect Coulomb corrections in $Z = 1$ targets, we use a factor $Z - 1$ rather than Z to account only for the additional charge in the nucleus compared to scattering from the proton or deuteron.

The central potential is an upper limit, as the potential is smaller everywhere else in the nuclear volume, so it is necessary to determine an appropriate average potential for scattering from the nucleus. This effect is incorporated in the EMA approach by an average potential 0.75-0.80 times the central potential, $V_{(0)}$ [91]. For E03103, we take $\Delta E = \overline{V} = 0.775 V_{(0)}$ and estimate this potential to be known at the 10% level. Note that Ref. [91] uses Z rather than $Z - 1$ in determining the average potential, but this has minimal impact on their extraction of the optimal potential, as this is obtained from calculations for heavy nuclei.

TABLE IV: The average effective potential ΔE and the values of the charge radii for the different targets used in the analysis. The radii for ^{3,4}He are measured values while the rest are calculated from the approximation $R_0(A) = 1.1\,A^{1/3} + 0.86\,A^{-1/3}$ [91].

Target	R_0 (fm)	ΔE (MeV)
^{3}He	2.32	0.66
^{4}He	2.17	0.77
^{9}Be	2.70	1.88
^{12}C	2.89	2.92
^{63}Cu	4.59	10.2
^{197}Au	6.55	19.9

In the EMA approach, the focusing factor of the incoming wave, $F_i = |(\vec{k}_i)_{\rm eff}|/|\vec{k}_i|$, enters quadratically in the cross section calculation and produces an enhancement

in cross section strength. However, the focusing factor of the outgoing wave cancels with the enhanced phase space factor in the effective cross section. The Coulomb correction factor in the EMA approach is given by the ratio of the model cross sections with nominal and shifted kinematics, scaled by the square of the focusing factor:

$$F_{\text{ccor}} = \frac{\sigma_{(E, E')}}{\sigma_{(E+\Delta E, \, E'+\Delta E)}} \left[\frac{E}{E + \Delta E} \right]^2, \qquad (22)$$

where the σs are the Born model cross sections. The measured cross sections are then multiplied by F_{ccor}, to get the Coulomb-corrected cross sections.
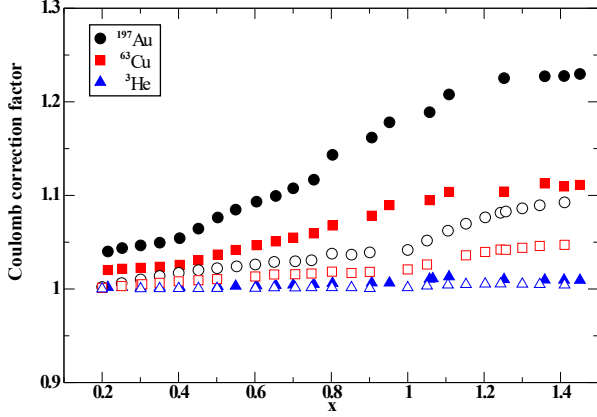
FIG. 9: Coulomb correction factors as a function of x for several targets as noted in the legend for a few selected kinematics for 5.776 GeV beam energy. The filled symbols show the correction for the 50 degree data while the open symbols represent 18 degree data.

Table IV shows the values for the RMS charge radii, and the magnitude of the average energy boost for the targets used in E03103. The Coulomb correction factors as applied to the data are shown in Figure 9. This figure shows the importance of the Coulomb distortion effects for the cross section and cross section ratio extractions in the medium energy range. These are relatively small for light nuclei, but for the heavy nuclei and near the quasi-elastic peak, these corrections are significant. The largest corrections are for the Au data at 40 and 50 degrees. With no Coulomb corrections applied, the EMC ratios are systematically 3-5% lower for the 50 degree data than the 40 degree data. After applying the EMA corrections described above, they are in excellent agreement, suggesting that the correction yields agreement at the 2% level or better, given the uncertainties in the comparison. This supports the idea that the EMA does a good job estimating this correction, though it assumes that no other effect modifies the cross section ratios in going from 40 to 50 degrees. This will be discussed further in Sec. V B.

Since this is a target- and x-dependent correction, neglecting the effect will modify both the extracted size of the EMC effect and the overall A dependence. In addition, for a given x value the angular dependence of the Coulomb correction factor implies a Q^2 dependence in the correction. Thus one should be careful about Q^2 averaging of the cross section or cross section ratios and the correction factor needs to be properly accounted for before applying such an averaging procedure. While Coulomb corrections were not applied to previous EMC measurements, the effect was estimated to be $\lesssim 3\%$ [4] for SLAC E139 [16], owing to the higher beam energy and smaller scattering angles. Nonetheless, neglecting this correction would imply some overestimate of the EMC effect in medium-heavy nuclei. We will discuss this further in the results section.

J. Isoscalar corrections

EMC ratios are expressed as the cross section ratio (per nucleon) of a target nucleus with an equal number of protons and neutrons (isoscalar nucleus) to that of deuterium. Thus, the EMC ratio for an isoscalar nuclei is just σ^A/σ^D. Since the protons and neutrons have different cross sections, the cross sections for nuclei with $Z \neq N$ will significantly differ from that of nuclei with $Z = N$. Thus, one typically applies a correction function to convert the measured F_2^A to a hypothetical isoscalar nucleus with the same mass number:

$$(F_2^p + F_2^n)/2 = f_{\text{iso}}^A (ZF_2^p + NF_2^n)/A. \qquad (23)$$

This correction function reduces to a function of F_2^n/F_2^p, the neutron to proton structure function ratios of the nucleus under investigation:

$$f_{\text{iso}}^A = \frac{(F_2^p + F_2^n)/2}{(ZF_2^p + NF_2^n)/A} = \frac{A(1 + F_2^n/F_2^p)}{2(Z + NF_2^n/F_2^p)}. \qquad (24)$$

The measured cross section ratios are multiplied by f_{iso}^A, which depends only on N, Z, and the neutron-to-proton structure function ratio, to get the isoscalar-corrected cross section ratios. Note that the structure functions in Eq. 23 correspond to the proton and neutron contributions to the heavy nucleus, as one is trying to convert from a non-isoscalar heavy nucleus to the isoscalar equivalent. In the past, these were simply replaced with the free neutron and proton structure function ratio.

There is significant uncertainty in the free neutron cross section in the large x region and so the extracted EMC ratios are sensitive to the choice of isoscalar correction factor. The F_2^n/F_2^p ratio has been extracted from proton and deuteron DIS measurements by SLAC [94] and NMC [95, 96]. Since there is no free neutron target, the extraction of F_2^n is always model-dependent. The SLAC extraction included Fermi motion while the NMC F_2^n/F_2^p ratios were extracted neglecting all nuclear effects (including binding) in the deuteron. The EMC effect results from SLAC E139 [16] took $\sigma_n = \sigma_p(1 - 0.8\,x)$ when
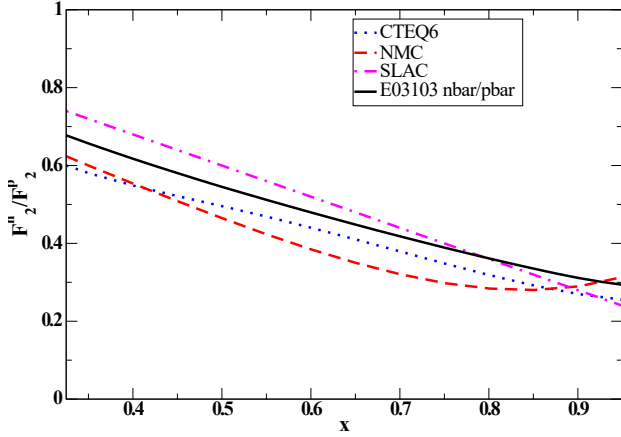
FIG. 10: (Color online) The ratio F_2^n/F_2^p vs. x for various parameterizations of the free nucleon structure functions along with the ratio of the smeared structure functions in deuterium [62, 93] extracted for the 40 deg kinematics of the E03013 experiment.
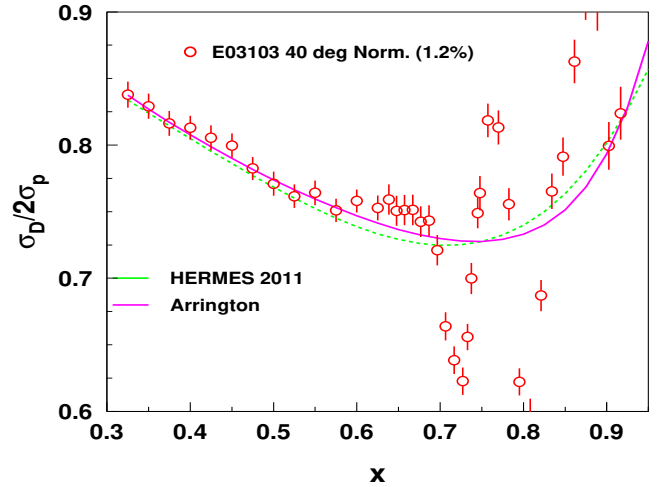

FIG. 11: (Color online) Our extracted $\sigma^D/2\sigma^p$ ratio along with calculations based on different F_2^n/F_2^p extractions (dashed line from [98] and solid line using [62, 93]). The structure above $x \approx 0.65$, is mainly due to the resonance in the proton structure function.

calculating the isoscalar correction. Figure 10 shows different representative parameterizations for F_2^n/F_2^p along with F_2^n/F_2^p constructed from parton distributions from CTEQ [97] computed at $Q^2 = 10$ GeV^2. The CTEQ fit also neglects the Fermi motion of nucleons. NMC mostly had data in the low x region, however, the x range covered by SLAC data is mainly in the large x region and overlaps with x range covered by E03103. All of these extractions are based on measurements of the deuteron-to-proton ratios in different Q^2 regions, and so any Q^2 dependence in the ratio would be expected to generate scatter in these results, beyond that associated with differences in the assumptions made in the extraction.

In our analysis we make a modified isoscalar correction. Instead of using free proton and neutron structure functions, we have used the contributions of F_2^p and F_2^n in ^{2}H, $\overline{F_2^n}$ and $\overline{F_2^p}$, in the above equation to correct the nuclear cross sections. As such, we are converting the deuteron structure in the denominator to a non-isoscalar deuteron, with the same Z/N ratio as the nucleus. The alternative would be to evaluate the neutron-to-proton ratio for all nuclei, which would involve significantly larger model dependence in heavier nuclei. In addition, we use the F_2^n/F_2^p ratio at the kinematics of our experiment, rather than taking the result from a high-Q^2 analysis. We determine the in-deuteron F_2^n/F_2^p ratio following the approach of Refs. [62, 93]. The extraction was performed taking the average of the values obtained using the different NN potentials and off-shell effects evaluated in Ref. [62], using the calculated value of $\overline{F_2^p}$ in the deuteron, and taking $\overline{F_2^n}/\overline{F_2^p} = (F_2^d - \overline{F_2^p})/\overline{F_2^p}$. This does not involve removing the nuclear effects to extract the free neutron structure function, as is usually the case, and so this procedure is somewhat less model dependent than the extraction of the free F_2^n/F_2^p ratio. We note that these analyses

also demonstrated that the model-dependence is smaller than assumed in some previous comparisons where the nuclear effects evaluated at a fixed Q^2 were applied to extract F_2^n/F_2^p spanning a range in Q^2. A similar result was seen in the analysis of the impact of nuclear effects on the extraction of the proton PDFs [61].

Figure 11 shows the $\sigma^D/2\sigma^p$ cross section ratios extracted from the E03103 data for the 40 degree kinematics. Representative extractions [62, 98] of the same ratio are also shown in the figure. It should be noted that the isoscalar correction depends on Q^2 [62, 93], and this effect is not negligible at large x. The correction factors derived using various parameterizations for ^{3}He and Au are shown in Figure 12.

In the case of ^{3}He, one can avoid the uncertainty associated with the isoscalar corrections by extracting the ratio of ^{3}He to $(^2$H+^{1}H). This ratio and the comparison to the isoscalar-corrected ^{3}He/^{2}H ratio are presented in section V B.

K. Scaling violation effects at high x

As discussed in Sec. I A, deviations from the scaling of the simple quark parton model arise due to QCD evolution of the PDFs, target-mass corrections which involve finite-Q^2 corrections to the approximations made in the infinite ν, Q^2 limit, and higher twist contributions which go beyond incoherent scattering from individual partons.

The kinematic effects due to target mass corrections were first calculated in the framework of the operator product expansion OPE in Ref. [99]. In the nucleon case, the measured structure function F_2^{meas} can be related to
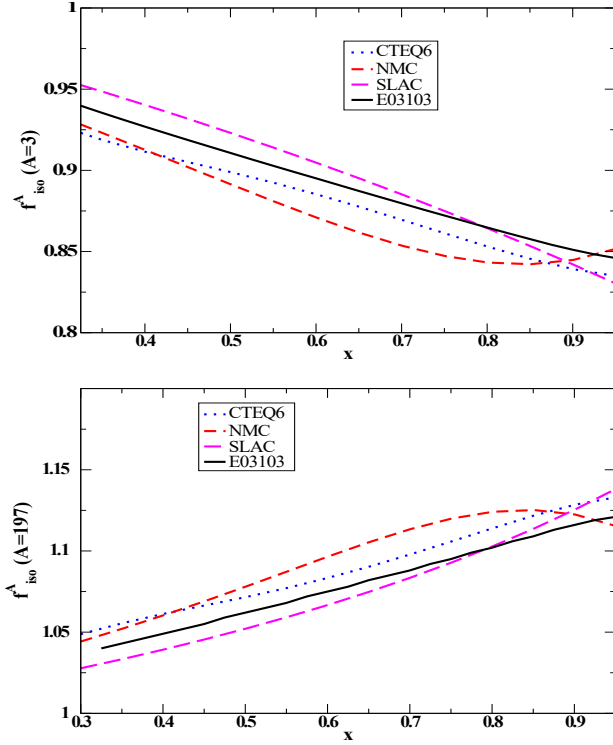
total systematic uncertainty in the cross section extraction is taken as the sum in quadrature of all systematic uncertainties of the quantities that contribute to the cross section. The components of the systematic uncertainty can be broadly divided into two groups: point-to-point uncertainties and normalization uncertainties. Point-to-point uncertainties are due to effects which may vary with time, kinematic conditions, or detector location, and so their effect is (or at least can be) uncorrelated between different data points. Normalization (scale) uncertainties affect the measurement globally (e.g., target thickness). Most corrections involve a mixture of point-to-point and normalization uncertainties. The resulting overall uncertainty in the cross section ratios is less than the total uncertainty in the cross section itself because many of the scale uncertainties and some point-to-point type errors cancel in the ratios. Table V summarizes the systematic uncertainties in extracting the cross section ratios. The dominant remaining contributions from the scale uncertainties are those associated with the absolute target thicknesses, radiative and background corrections. These range from 1.5–2.0% on the EMC ratios, and are provided for each target ratio in the supplementary data tables [106]. Individual contributions are discussed below.

TABLE V: Typical sources and magnitude of the systematic uncertainties in extracting cross section ratios. These are added in quadrature with the statistical uncertainties to get the total random uncertainties.

Item	Absolute uncertainty($\pm$)	$\delta R/R$ ($\pm\%$)
Beam Energy (offset)	5×10^{-4}	–
Beam Energy (tgt-dep)	2×10^{-4}	0.08
HMS Momentum (offset)	5×10^{-4}	–
HMS Momentum (tgt-dep)	2×10^{-4}	0.0-0.12
HMS angle (offset)	0.5 mr	–
HMS angle (tgt-dep)	0.2 mr	0.29-0.60
Beam Charge	0.5%	0.31
Target Boiling	0.45%	0.0-0.1
End-cap Subtraction	2–3%	0.28-0.45
Acceptance	1%	0.3
Tracking Efficiency	0.7%	0.3
Trigger Efficiency	0.3%	0.0
Electronic Dead Time	0.06%	0.0
Computer Dead Time	0.3%	0.3
Charge Symmetric BG		0.0-1.0
Coulomb corrections	0.2%	0.1
Pion Contamination	0.2%	0.1
Detector Efficiency	0.2%	0.0
Radiative Corrections	1%	0.5
Bin-centering	0.2%	0.1
Quadrature sum		0.90-1.11

Kinematic offsets in the beam energy, spectrometer momentum, and spectrometer angle can yield errors in our extracted cross sections. We use our model cross section to assess the uncertainty in the cross sections due to these effects. The cross section ratios, however, are largely insensitive to such offsets.

The point-to-point uncertainty in the beam charge measurement was estimated to be 0.5% via studies of the residuals to calibration fits taken throughout the experiment. A scale uncertainty of 0.2% was assumed for the charge measured, due to the uncertainty in the calibration against the UNSER parametric beam current calibration [83].

As mentioned in section II B, thicknesses of the solid targets were calculated using measurements of the mass and area of the targets. Thicknesses of the cryotargets were computed from the target density and the length of the cryogen in the path of the beam. The absolute uncertainty in the ^{2}H thickness is estimated to be 1.29%. When comparing to other cryogenic targets, part of this uncertainty cancels and the overall uncertainty in the cross section ratio (A/D) is 1.59% and 1.29% for ^{3}He/D and ^{4}He/D respectively. For heavy nuclei, the scale uncertainty in the cross section ratio due to target thickness is found to be between 1.4% to 2.4%. In addition to the nominal target densities, there are corrections associated with beam heating effects and fluctuations in the pressure and temperature. The uncertainty associated with this correction comes from the uncertainties in the fits to target luminosity scans. Though no boiling correction is made in the case of the deuterium target, the uncertainty from the luminosity scan data is still included in the A/D ratios. We assign a scale uncertainty of 0.24% (solid targets) to 0.38% (helium targets) for the target ratios.

The scale uncertainty of the acceptance in the HMS was estimated to be 1% from the elastic cross section studies, while the point-to-point uncertainty comes from the comparison of the model in the inelastic region (where the cross section is smoothly varying) to data, and is estimated to be 0.5%. In the cross section ratios, these uncertainties partially cancel. The scale uncertainty in the solid target ratios is estimated to be 0.5% and 0.2% for helium target ratios. The point-to-point uncertainty is estimated to be 0.3% for both.

The normalization uncertainty of the tracking efficiency is determined to be 0.7%, mainly due to the limitations of the algorithm used for tracking and the efficiency calculation algorithm. A point-to-point uncertainty of 0.3% is assigned to the tracking efficiency in the target ratios, primarily due to differences in rates between the targets.

At very low x values, the structure functions are expected to scale, and any deviation is possibly due to the charge symmetric background (since this is the dominant uncertainty for heavy nuclei at small x and large scattering angles). A comparison of 40 and 50 degree data suggests that scaling is satisfied if the CSB varies by no more than 5%. A polynomial fit was made to the

charge symmetric background as a function of x, and 5% of the magnitude of the charge symmetric background is applied as the point-to-point uncertainty in the charge symmetric background subtraction.

The model dependence in the radiative correction was studied by varying the strength of the DIS and QE contributions to our model independently, and by comparing to a completely independent fit by Bosted and Mamyan [107]. The change in extracted cross section was rather pronounced in the low x region when comparing to the Bosted-Mamyan fit (several percent for heavier nuclei). This was primarily due to contributions to the radiative tail from the QE process. Investigations comparing the QE cross section used in the model described here and the Bosted-Mamyan fit showed similar levels of agreement with existing data at low Q^2, although both models displayed deviations at the 10% level. In the end, the final results were generated by taking the average of the target ratios generated with both models with an additional (correlated) x-dependent uncertainty added due to the difference in the models. In addition to this x-dependent uncertainty (coming from differences in the QE model), an additional 1% uncertainty in the cross section is assigned due to the inelastic model, and additional point-to-point uncertainties are assigned to account for kinematic dependent differences. The point-to-point uncertainty for the target ratios is estimated to be 0.5%. An additional scale uncertainty, associated with the difference in radiation lengths between the targets, is taken to be 0.1% except for the high-radiation length targets (Cu and Au) for which it is 1%.

The efficacy of the model used to describe the Monte Carlo yield across the acceptance of the spectrometer was studied by varying the shape of the model. This is done by supplying artificial x and Q^2 dependencies as input to the individual DIS and QE pieces in the model cross section. The variation was found to be most pronounced for the $x > 0.8$ region, and we estimate a point-to-point uncertainty of 0.2% for the cross sections, and 0.1% for the cross section ratios. Uncertainties in the Coulomb corrections are mainly due to the knowledge of the energy shift, ΔE, used in the EMA calculation. We estimate this to be known at the 10% level. For the Au target at 40 degrees, this uncertainty ranged from 0.5% at low x to 1.5% at high x.

V. RESULTS AND DISCUSSION

Before presenting the results, it is instructive to compare our kinematics to the earlier SLAC experiments. This will help identify potential issues in the comparison of the EMC ratios and elucidate the possible role of the Q^2 dependent effects when comparing data from different experiments. Figure 14 shows kinematics for our measurement and SLAC E139 and E140, as well as the recent results from CLAS.

E03103 took data on all targets at 40° and 50°, and

the cross section ratios with respect to deuterium were extracted. The EMC ratios are extracted from the 40 degree angle (solid line in Fig. 14) where the data have better statistics and more complete kinematic coverage. Data were also collected for a detailed Q^2 dependence study at 8 additional kinematic settings on C and ^{2}H.
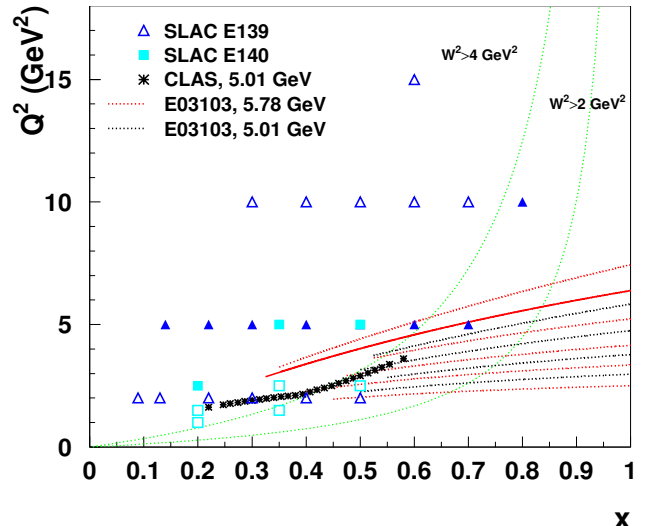

FIG. 14: (Color online) The E03103 kinematics, indicated with dashed and dotted lines, along with the SLAC experiments E139 [16] (triangles) and SLAC E140 [108] (squares). Kinematics are shown for the target with maximum coverage (Fe for the SLAC measurements, C for E03103). The solid line and filled symbols represent the kinematics used in the main comparison of the results. Contours of constant invariant mass squared are also shown in the figure.

In the cross section ratio plots, representative world data is displayed with the corresponding nuclei where available. In the kinematics comparison plot we chose to display kinematics of SLAC experiments because of the overlap in kinematics with our experiment at high x. For comparison of the EMC ratios we use the SLAC data averaged over all Q^2 values at each x; note that at the highest x measured by SLAC ($x = 0.8$), only $Q^2 = 10$ GeV^2 is available. For each x, Q^2 value, the published SLAC E140 results are averaged over several ϵ points - this point is addressed later in this section.

To be consistent, the SLAC data are presented with updated Coulomb and isoscalar corrections using the same prescriptions used for the analysis of E03103 data. The updated data points and corrections factors are available in the supplementary online material [106].

A. Q^2 dependence of the ratios

The scaling of the structure functions for nucleons is expected to hold in the conventional DIS region ($W^2 > 4$ and $Q^2 > 1$), where the non-perturbative, resonance structure is no longer apparent and QCD evolution is
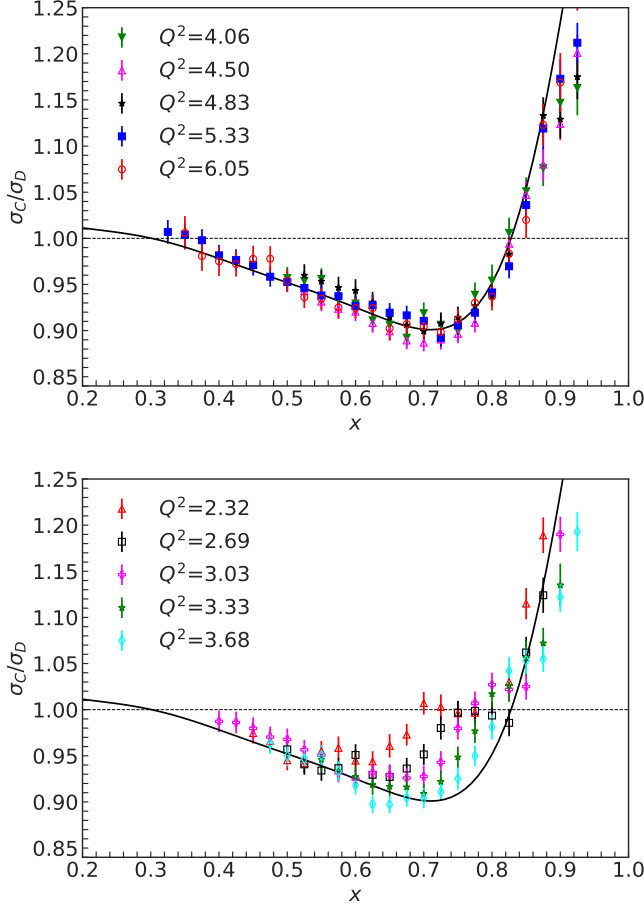
FIG. 15: (Color online) Ratio of C and ^{2}H cross sections for the five largest Q^2 (top panel) and five lowest Q^2 (bottom panel) settings as a function of x. Uncertainties are the combined statistical and point-to-point systematic. The Q^2 values quoted are for $x = 0.75$, and the data labeled Q^2=5.33 correspond to our primary results, taken at 40°. The solid black line is the SLAC parameterization of the EMC effect for carbon [16].

and the scatter at the largest x values is consistent with the uncertainties in the individual measurements. This suggests that any Q^2 dependence in the structure function is either small or cancels in the target ratios. The bottom figure shows the low Q^2 measurements, where there is a clear difference in the Q^2 dependence of carbon and deuterium below $Q^2 \approx 3$ GeV^2 and $x > 0.6$, corresponding to W^2 values below 2–3 GeV^2, where one expects large resonance contributions.
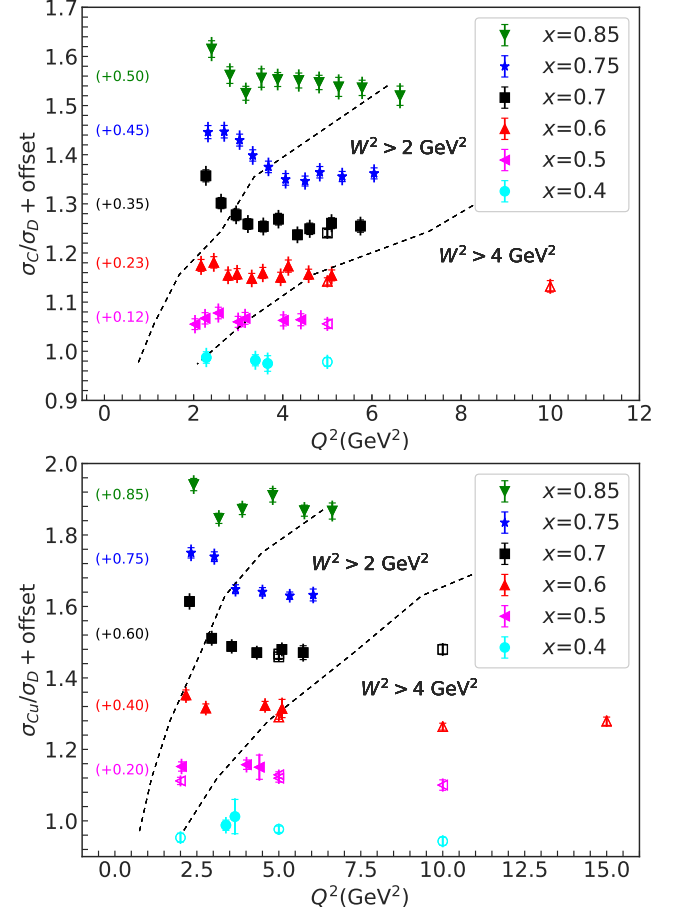

FIG. 16: (Color online) EMC ratios for C (top) and Cu and Fe (bottom) as a function of Q^2 at fixed x values as indicated in legend. For clarity, an additive offset is applied along the y axis. Open symbols are from updated SLAC E139 [16] results while the closed symbols are E03103 values. Inner error bars show the combined statistical and point-to-point systematic while the outer error bars represent the total uncertainty including the normalization uncertainties. The dashed lines indicate the values of $W^2 = 2, 4$ GeC^2 for each x value.

the only source of Q^2 dependence. At smaller values of W^2, corresponding to large x, additional scaling violations can originate from resonance contributions. For E03103, the data are in the conventional DIS region up to $x \approx 0.6$. There are indications [4] that the nuclear structure functions in the resonance region, down to very low W^2 values ($W^2 > 1.5$ GeV^2 for $Q^2 > 3$ GeV^2), shows the same global behavior as in the DIS region. Therefore, we took data at large x extending below $W^2 = 4$ GeV^2, and made detailed measurements of the Q^2 dependence of the ratios to ensure that there was no indication of any systematic deviation from the DIS limit.

The EMC ratios for carbon at several Q^2 values are compared in Fig. 15. The top panel shows the EMC ratios for the five highest Q^2 settings from our experiment, along with the fit to the EMC effect from [16]. The data do not show any systematic Q^2 dependence,

Figure 16 shows the Q^2 dependence of the structure functions for C (top) and Cu or Fe (bottom) at several x values, to allow for a more careful examination of the Q^2 dependence as a function of x. The carbon data have additional Q^2 values for E03103, due to the data taken using a lower beam energy, while the Cu data have more high-Q^2 data from the SLAC measurements. There is a fair agreement with the SLAC data over the kinematic re-

gions where data are available, and clear deviations from a constant ratio are visible below $Q^2 = 4$ GeV^2 and at large x values.
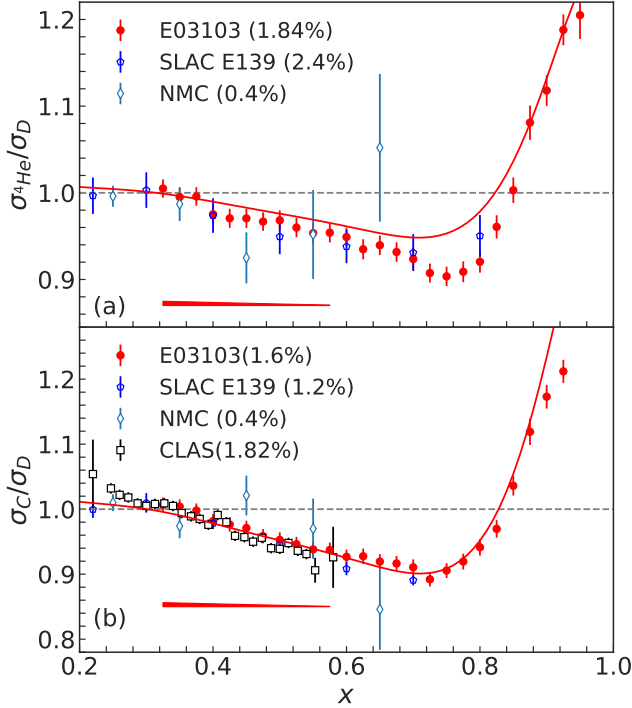
B. x dependence of the ratios

FIG. 17: (Color online) EMC ratios for ^{4}He (a) and ^{12}C (b) as a function of x for the 40 degree results. Error bars show the combined statistical and point-to-point systematic uncertainties. The solid error band denotes the correlated uncertainty due to the size of the quasielastic tail in the radiative corrections; overall normalization uncertainties are shown in the parenthesis. Also shown are the updated SLAC E139 [16] and NMC data [18, 19]. The solid curves show the A dependent fit to the EMC effect from [16].

We now examine the x dependence of the EMC ratios for all of the targets from E03103, SLAC, and CLAS, including Coulomb corrections and our updated isoscalar corrections. We first discuss the cross section ratios for C and ^{4}He, as these ratios have no isoscalar correction, and the Coulomb distortion effects are small (<1%) for these nuclei. Figure 17 shows the cross section ratios for ^{4}He and ^{12}C, along with the updated SLAC E139 data and the NMC data [18, 19]. Note that the red curve is a global fit to the A dependence from SLAC [16], which yields a smaller EMC effect for ^{4}He than seen in their data or our updated measurement. CLAS results [105] are also shown for carbon. There is overall good agreement between the data sets. Both the CLAS and E03103 results are of high precision, with E03103 extending to

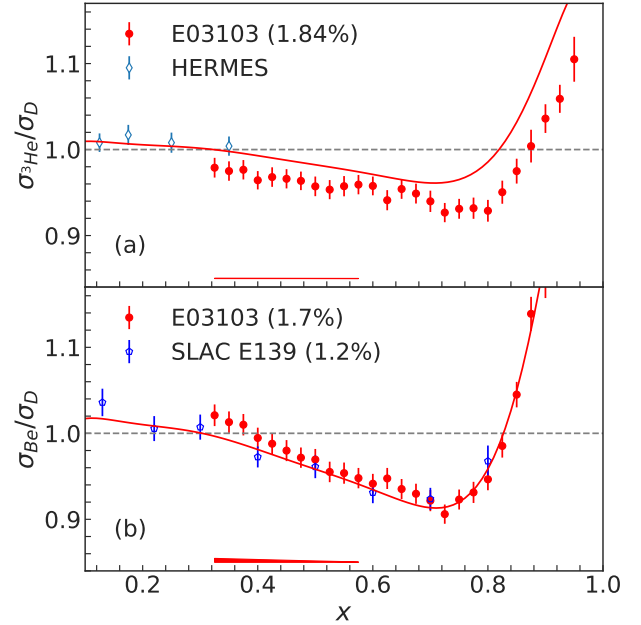larger x, although at a lower W^2 than previous measurements.

FIG. 18: (Color online) Isoscalar EMC ratios for ^{3}He (a) and ^{9}Be (b) for the 40 degree data. Uncertainties are as described in Fig. 17. Also shown are the HERMES ^{3}He data [20, 21] (updated to include our modified isoscalar correction). The solid curve shows an A dependent parameterization [16] for the EMC effect.

Figure 18 shows the cross section ratios for ^{3}He and ^{9}Be. Both of these nuclei are light enough that the Coulomb corrections are small, but require a proton (neutron) excess correction to obtain the isoscalar EMC ratios (see section III J). The magnitude of this correction is significant for ^{3}He, ranging from about 5% to 15% for our kinematics. For ^{9}Be, the correction is of the opposite sign and roughly a factor of three smaller. The ^{3}He EMC ratios exhibit the general shape observed for the cross section ratios for heavy nuclei.

One can avoid the uncertainty associated with the isoscalar correction, and thus better evaluate models of the EMC effect, by taking the ratio of ^{3}He to (^{2}H+^{1}H) which allows comparisons to calculations that are independent of the neutron structure function. These ratios are extracted for our 40 degree setting and shown in Figure 19 (red squares), along with the isoscalar-corrected ^{3}He/^{2}H ratios (blue circles). The isoscalar-corrected ^{3}He/^{2}H ratio and the ^{3}He/(^{2}H+^{1}H) results are in good agreement below $x \approx 0.65$, but the resonance structure at large x in the proton is not washed out, and so the extended scaling observed in nuclei [4] is not as effective, limiting the useful range for this ratio to $x \lesssim 0.65$.

Next, we examine the ratios for heavy nuclei in Fig. 20. Several corrections to the data on heavy nuclei are larger or more uncertain than for light nuclei. At low x, the
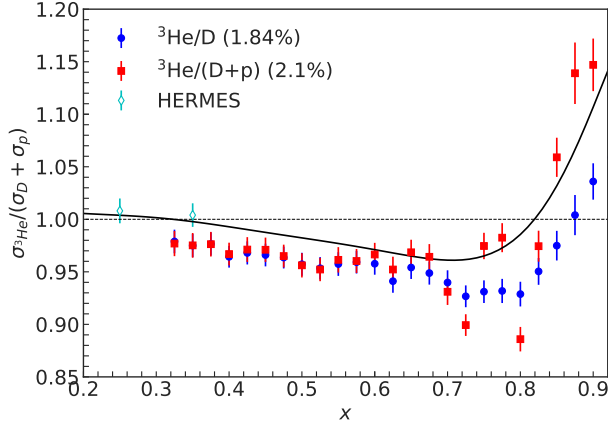
FIG. 19: (Color online) Comparison of the isoscalar-corrected ^{3}He/D ratio (blue circles) to ^{3}He/(D+p) (red squares). The agreement is very good below $x = 0.65$ (which corresponds to $W \approx 1.9$ GeV). At larger x, the resonance structure in the free proton is evident.

FIG. 20: (Color online) EMC ratios for Fe and Cu (a) and for Au and Pb (b) as a function of x for the 40 degree data. Uncertainties are as described in Fig. 17. The SLAC E139 and E140 data include updated Coulomb and isoscalar corrections, while the CLAS data has been updated with isoscalar corrections only since Coulomb corrections had already been applied. BCDMS [109] Fe results are shown as published.

radiative corrections and charge symmetric background (see section III C 2) are quite large. At high x, Coulomb distortion becomes large for high-Z targets; the correction for Au ranges from 3% at low x to 12% at high x values for the 40° data.

Taking normalization uncertainties into account, our large-x results are in generally good agreement with the SLAC data, although the SLAC ratios at $x = 0.8$ are always slightly higher than our results. This is possibly because the $x = 0.8$ SLAC points were taken at higher Q^2 values ($Q^2 = 10$ GeV^2) than the E03103 data ($Q^2 \approx 6$ GeV^2), leading to a noticeable difference between the target mass corrections needed for the two data sets. Figure 21 shows the points plotted as a function of x (left panels) and ξ (right panels), where plotting the ratio vs. ξ provides the dominant part of the target mass correction. The target mass correction shifts all points lower values of ξ with the largest shifts occurring at large x. When plotted as a function of ξ, the EMC ratios are consistent within the scale uncertainties.

At small x values, we find systematic disagreements with the SLAC measurements. While the light isoscalar nuclei are in relatively good agreement with the E139 results, the ^{3}He ratios are systematically lower than HERMES for $x \leq 0.4$ (although the region of overlap is small), and the very heavy nuclei are systematically higher. Given the normalization uncertainties, it is difficult to conclude that there is a true inconsistency between the data sets, but we examine the pattern of disagreement to evaluate possible explanations for the small differences.

First, note that these nuclei have large isoscalar corrections, which are of the opposite sign for ^{3}He and the heavy nuclei. However, the low-x region has the least uncertainty in the ratio of F_2^n/F_2^p [61, 62], and the correction becomes smaller at low-x values, where the F_2^n/F_2^p
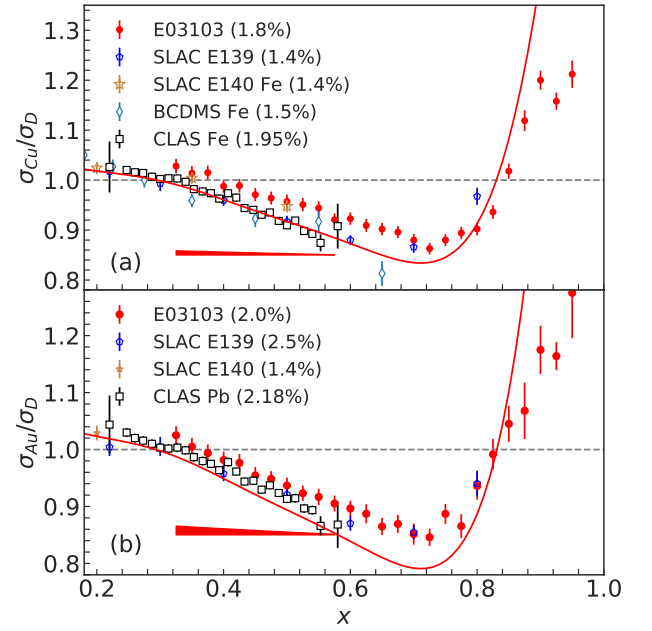
becomes closer to unity. In addition, the SLAC data as presented here include the updated isoscalar correction that we apply to our data, and thus such a discrepancy would have to be associated with the Q^2 dependence of the isoscalar correction. It therefore seems unlikely that it could be responsible for the difference between data sets at small x.

The heavy nuclei also have significant corrections due to Coulomb distortion, radiative corrections, and charge-symmetric backgrounds. The charge-symmetric background is directly measured for all nuclei so it is unlikely this is the source of the discrepancy. It is interesting to note that while effects due to Coulomb distortion tend to be smaller at low x, the agreement between the E03103 and SLAC results for heavy targets is apparently better with no Coulomb corrections applied to either data set.

Since the Coulomb correction factors (see section III I) are substantial for the heavy nuclei, it motivated us to further investigate the details of this correction; in particular the impact of its strong angular dependence. This angular dependence could potentially affect the apparent ϵ dependence of the cross section ratios. As mentioned in the introduction, the identification of the cross section ratio with the F_2 ratio, and thus the EMC effect, is valid only if $\epsilon = 1$ or $R_{A_1} = R_{A_2}$ (identical ratio of longitudinal to transverse virtual-photon absorption cross section for the two nuclei). This idea was tested by SLAC
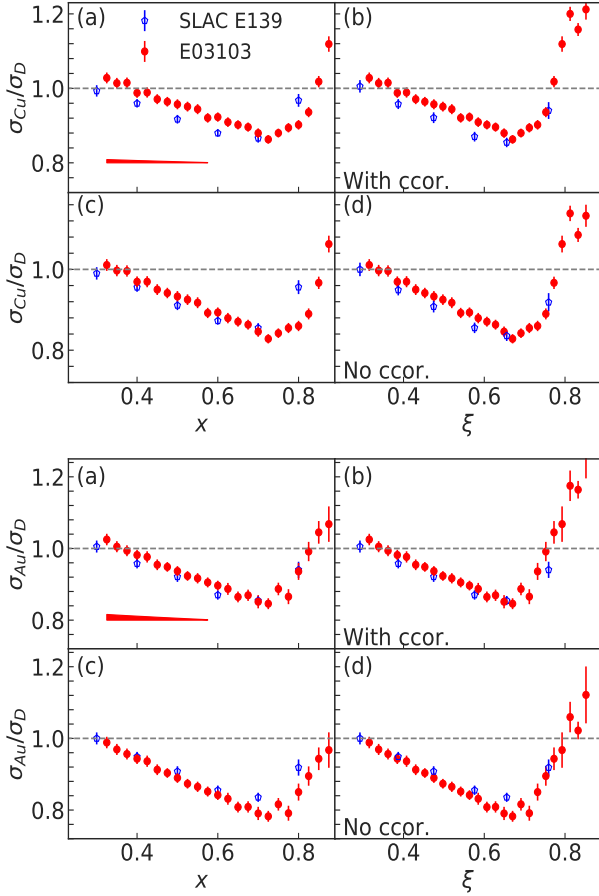
FIG. 21: (Color online) EMC ratios for our Cu and Au data compared to the SLAC Fe and Au data, respectively, shown using four different sets of corrections. The panels on the left (right) side show the ratio vs x (ξ), while the panels on the top (bottom) show the ratios with (without) Coulomb corrections applied. For each target, panel (b) shows the comparison where one expects the best agreement between different measurements, assuming that the Coulomb and so-called target mass corrections account for any θ and Q^2 dependence in the cross section ratios. For all nuclei, high-x SLAC and JLab results are in good agreement, after taking into account the scale uncertainties in the measurements.
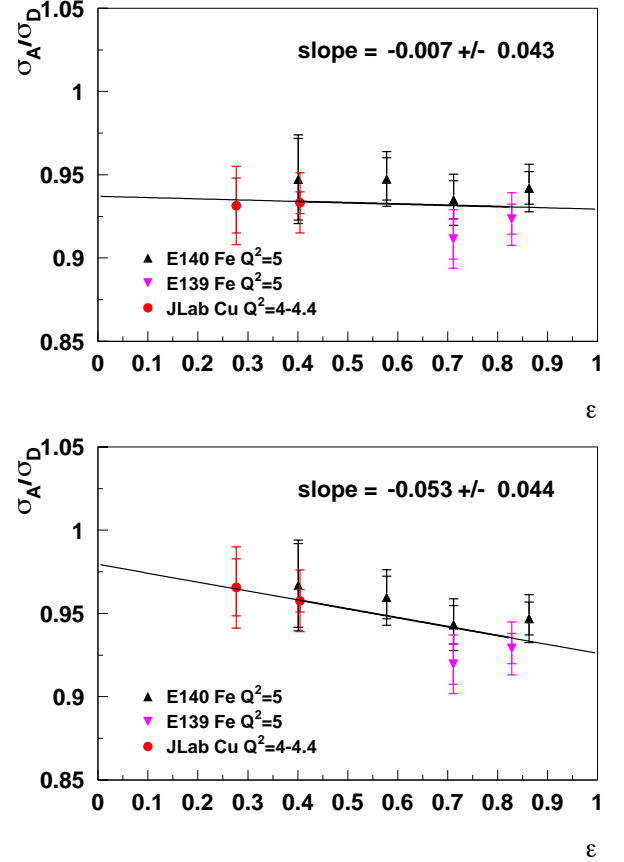

FIG. 22: (Color online) Extracted cross section ratios using the updated data from [16, 108] and E03103 experiment as a function of ϵ for the Fe/Cu targets for $x = 0.5$ and Q^2 values as mentioned in the legend. The top (bottom) plot shows the target ratio without (with) Coulomb corrections applied. Inner error bars denote statistical and point-to-point uncertainties combined in quadrature while out error bars include contributions from normalization uncertainties. The uncertainty on the slope is calculated from point-to-point errors as well as the experiment-dependent normalization uncertainties.

E140 [108], which set limits on any possible nuclear dependence for R. They assumed the Coulomb distortion effects were small and did not include these corrections in their analysis. However, a re-examination of the SLAC 140 [108], SLAC E139 [16] (including updated Coulomb and isoscalar corrections) and preliminary results for the Cu target from E03103 data suggested a non-zero nuclear dependence in $R_A - R_D$ [110].

Here we present an updated version of the analysis initially performed in [110]. Figure 22 shows the ϵ dependence of the extracted cross section ratios for the Cu (Fe target for the SLAC experiments) target extracted for $x = 0.5$, $Q^2 \sim 5$ GeV^2 point. In this analysis, the data at low ϵ values from the E03103 experiment are combined with the measurements from SLAC [16, 108] to study the ϵ dependence of the cross section ratios. The slope derived using a linear fit after accounting for the appropriate normalization uncertainties between different experimental data sets is found to be consistent with zero (see top plot in figure 22). However, after the application of Coulomb corrections there is a change in the slope (from -0.007±0.043 to -0.053±0.044). This analysis hints at the interesting possibility that there may be a non-trivial ϵ dependence for the cross section ratios, implying a detectable nuclear dependence of $R = \sigma_L/\sigma_T$ at large x.

There have been other indications of possible A dependence to R [111–114]. These previous results are consistent with a decrease in R for nuclei with more neutrons, which could explain the observation of an increase

in σ_A/σ_D for ^{3}He and a decrease for heavier nuclei with a significant neutron excess. However, we cannot exclude the possibility that these features are the result of errors in our knowledge of the thickness of these targets which give shifts in the ratios which happen to vary with the N/Z ratio of the nucleus. More definitive information with respect to a possible A dependence of R will be forthcoming in the final analysis of Hall C experiments E02109 [115] and E04001 [116], which took data primarily (although not exclusively) in the resonance region, and the future E12-14-002 [117], which will emphasize measurements in the DIS region.

C. A dependence of the EMC effect

The overall size of the EMC effect is parameterized in terms of the x dependence (slope) of the EMC ratios, $R_{\mathrm{EMC}}(x)$. Table VI shows the EMC slopes, $|dR_{\mathrm{EMC}}/dx|$ for $0.3 < x < 0.7$, extracted from data from SLAC, CLAS and this experiment. This table is an updated version of table 1 provided in [36] which includes some of the updated results from E03103 as well as the recent CLAS data [105]. The slopes are shown vs. A in Fig. 23. The CLAS slopes are systematically higher than those from the other experiments. This, combined with the fact that CLAS does not provide results on nuclei lighter than carbon, means that a combination of the slopes for all nuclei (or $A \geq 4$) will yield a larger A dependence than any of the individual data sets. Each experiment uses a single deuteron data set for all A/D ratios, so the deuteron uncertainties should be treated as a common normalization uncertainty for all ratios from a given experiment in a complete analysis of the A dependence.
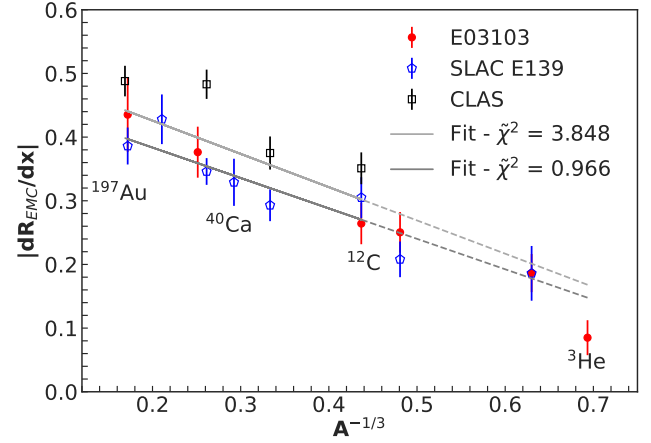

FIG. 23: (Color online) EMC slope vs. A for JLab E03103 (this work), SLAC E139 [16], and CLAS [105]. The linear fit excludes $A < 12$ nuclei, with the upper fit (and reduced χ^2 value including all data sets, and the lower excluding the CLAS data.

TABLE VI: EMC slopes extracted from SLAC [16, 36], CLAS [105], and this experiment. Slopes are extracted using consistent isoscalar corrections for all three experiments, and with Coulomb corrections applied to all three data sets.

A	JLab E03103	SLAC E139	CLAS
^{3}He	0.085 ± 0.027	-	-
^{4}He	0.186 ± 0.030	0.186 ± 0.043	-
^{9}Be	0.250 ± 0.032	0.208 ± 0.028	-
^{12}C	0.264 ± 0.033	0.305 ± 0.032	0.351 ± 0.025
^{27}Al	-	0.293 ± 0.025	0.375 ± 0.026
^{40}Ca	-	0.329 ± 0.037	-
^{56}Fe	-	0.346 ± 0.021	0.483 ± 0.023
^{63}Cu	0.376 ± 0.040	-	-
^{107}Ag	-	-	-
^{197}Au	0.435 ± 0.059	0.386 ± 0.029	-
^{208}Pb	-	-	0.488 ± 0.024

It is not clear why the CLAS EMC ratios yield larger slopes. This data set is taken at lower Q^2 than the E03103 and SLAC data, but target mass corrections yield a larger slope (when fitting $F_2^{(0)}(x)$ rather than $F_2(x)$), and this increase is largest for CLAS because it is at lower Q^2. So applying target mass corrections would only increase the discrepancy between CLAS and the higher-Q^2 data sets. Ref. [105] extracts the EMC ratios with a Q^2 cut of $Q^2 > 1.5$ GeV^2, but also examines the impact of other cuts. In their analysis requiring $Q^2 > 2.0$ GeV^2, the average slope is decreased by 0.02 with little impact on the uncertainties, while $Q^2 > 2.5$ GeV^2 decreases the average slope by 0.035 but with much larger uncertainties. This suggests that inclusion of the lower Q^2 data may be increasing the slope, but it is difficult to quantify exactly how this impacts the comparison to the SLAC and JLab E03103 measurements.

Radiative corrections may also play a role in the difference in the CLAS EMC slopes. While CLAS, E03103, and SLAC all treat radiative effects based on the Mo and Tsai formalism [88], the detailed implementation and the cross section models used differ. The radiative corrections program used by E03103 is based on that used for the earlier SLAC analysis, while CLAS uses the program described in [118]. In particular, it is possible that differing approximations in the two approaches may result in systematic differences in the cross section and EMC slopes which can have a significant impact at smaller x values.

The measurements on light nuclei, in particular for ^{9}Be, show a clear deviation from scaling with density [57], while the lightest nuclei show deviations from a smooth scaling with A. It has been suggested that the local density or the overlap of the struck nucleon with nearby neighbors may drive the scaling of the EMC effect [36, 57, 119], or that off-shell effects in the highly virtual nucleons may in fact be responsible [34, 105]. In connection with these ideas, it has been suggested that

there may be both an A dependence and an isospin dependence, with additional modification in neutron-rich nuclei [36, 120, 121]. So far, examinations of the A dependence of the EMC ratios under different assumptions about the isospin dependence are inconclusive, with the data being consistent with a significant flavor dependence based on the isospin structure of SRCs [105], but somewhat better described under the assumption of isospin independence [36, 119]. The additional data on heavy nuclei presented here and the small changes in the results for light nuclei do not significantly impact the conclusions of such comparisons, as a larger range of N/Z is needed to increase the sensitivity [122].

VI. CONCLUSIONS

Deep inelastic scattering from ^{1,2}H, ^{3,4}He, Be, C, Cu, and Au targets was measured by the E03103 experiment at Jefferson Lab. The ratios of inclusive nuclear cross sections with respect to the deuterium cross section have been determined for $x > 0.3$ for Q^2 values between 3 and 8 GeV^2. We include new data on heavy nuclei, not included in the original results [57], and provide a combined analysis of our results with previous SLAC measurements [16] and recent CLAS data [105], applying consistent isoscalar and Coulomb corrections to the different data sets.

E03103 addressed several of the limitations of previous measurements. We have provided benchmark data for calculations of the EMC effect in light nuclei. Predicted deviations from the x dependence observed in heavy nuclei [73, 74] were not observed in ^{3}He and ^{4}He, but clear deviations from the simple assumption of mass or density scaling of the EMC effect are observed. At large x, where binding and Fermi motion effects dominate, our new data for light and heavy nuclei can serve as a baseline for traditional nuclear physics calculations, including several few-body nuclei where structure related uncertainties are minimal.

The data presented in this work will bridge the gap between measurement of the EMC effect in light nuclei and medium heavy nuclei, thus providing a comprehensive basis to test state of the art models that attempt to explain the observed nuclear dependence. For the moment, few models provide an explicit prediction for the A dependence, thus limiting the ability to directly constrain these models without further effort on the theory side.

While these data provide important new information about the EMC effect, there are still limitations on how well these results could be used to constrain explanations of the EMC effect. Some of these limitations will be addressed by 12 GeV experiments at Jefferson Lab [122, 123]. This will provide further information on the detailed behavior of the observed nuclear nuclear dependence with an expanded set of light nuclei, including nuclei with significant cluster structure and medium-to-heavy nuclei covering a range of N/Z to increase sensitivity to flavor-dependent effects.

[1] J. Aubert et al. (European Muon Collaboration), Phys. Lett. **B123**, 275 (1983).

[2] J. D. Bjorken, Phys. Rev. **179**, 1547 (1969).

[3] I. Schienbein et al., J. Phys. **G35**, 053101 (2008).

[4] J. Arrington, R. Ent, C. E. Keppel, J. Mammei, and I. Niculescu, Phys. Rev. C **73**, 035205 (2006).

[5] I. Niculescu, J. Arrington, R. Ent, and C. Keppel, Phys.Rev. **C73**, 045206 (2006).

[6] S. V. Akulinichev, S. Shlomo, S. A. Kulagin, and G. M. Vagradov, Phys. Rev. Lett. **55**, 2239 (1985).

[7] A. Bodek and J. Ritchie, Phys. Rev. D **23**, 1070 (1981).

[8] A. Bodek and J. Ritchie, Phys. Rev. D **24**, 1400 (1981).

[9] L. Frankfurt and M. Strikman, Nucl. Phys. **B181**, 22 (1981).

[10] J. Ashman et al., Phys. Lett. B **202**, 603 (1988).

[11] J. Ashman et al., Z. Phys. C **57**, 211 (1993).

[12] G. Bari et al., Phys. Lett. B **163**, 282 (1985).

[13] A. Bodek et al., Phys. Rev. Lett **51**, 534 (1983).

[14] S. Stein et al., Phys. Rev. D **12**, 1884 (1975).

[15] A. Bodek et al., Phys. Rev. Lett **50**, 1431 (1983).

[16] J. Gomez et al., Phys. Rev. D **49**, 4348 (1994).

[17] J. Aubert et al. (European Muon Collaboration), Nucl. Phys. **B272**, 158 (1986).

[18] M. Arneodo et al., Nucl. Phys. **B441**, 12 (1995).

[19] P. Amaudruz et al., Nucl. Phys. **B441**, 3 (1995).

[20] K. Ackerstaff et al., Phys. Lett. **B475**, 386 (2000).

[21] A. Airapetian et al., Phys. Lett. B **567**, 339 (2003).

[22] A. Antonov and I. Petkov, Il Nuovo Cimento A **94**, 68 (1986).

[23] I. Sick and D. Day, Phys. Lett. **B274**, 16 (1992).

[24] D. F. Geesaman, K. Saito, and A. W. Thomas, Ann. Rev. Nucl. Part. Sci. **45**, 337 (1995).

[25] P. R. Norton, Rept. Prog. Phys. **66**, 1253 (2003).

[26] M. M. Sargsian et al., J. Phys. **G29**, R1 (2003).

[27] S. Malace, D. Gaskell, D. W. Higinbotham, and I. Cloet, Int. J. Mod. Phys. E **23**, 1430013 (2014), 1405.1270.

[28] N. Fomin, D. Higinbotham, M. Sargsian, and P. Solvignon, Ann. Rev. Nucl. Part. Sci. **67**, 129 (2017), 1708.08581.

[29] D. M. Alde et al., Phys. Rev. Lett. **64**, 2479 (1990).

[30] J. Smith and G. Miller, Phys. Rev. C **65**, 055206 (2002).

[31] G. A. Miller and J. R. Smith, Phys. Rev. C **65**, 015211 (2002), [Erratum: Phys.Rev.C 66, 049903 (2002)], nucl-th/0107026.

[32] O. Benhar, V. R. Pandharipande, and I. Sick, Phys. Lett. B. **410**, 79 (1997).

[33] S. A. Kulagin and R. Petti, Nucl. Phys. **A765**, 126 (2006).

[34] L. Weinstein, E. Piasetzky, D. Higinbotham, J. Gomez, O. Hen, and R. Shneor, Phys. Rev. Lett. **106**, 052301 (2011).

[35] O. Hen, E. Piasetzky, and L. B. Weinstein, Phys. Rev. C **85**, 047301 (2012), 1202.3452.

[36] J. Arrington et al., Phys. Rev. C **86**, 065204 (2012).

[37] L. Frankfurt and M. Strikman, Phys. Rev. C **82**, 065203 (2010), 1009.4920.

[38] L. Frankfurt and M. Strikman, Int.J.Mod.Phys. **E21**, 1230002 (2012).

[39] R. L. Jaffe, Phys. Rev. Lett. **50**, 228 (1983).

[40] H. J. Pirner and J. P. Vary, Phys.Rev. **C84**, 015201 (2011).

[41] M. Bashkanov, S. J. Brodsky, and H. Clement, Phys. Lett. B **727**, 438 (2013), 1308.6404.

[42] J. R. West, S. J. Brodsky, G. F. de Teramond, A. S. Goldhaber, and I. Schmidt (2020), 2004.14659.

[43] J. Arrington (2006), nucl-ex/0602007.

[44] N. Fomin et al., Phys. Rev. Lett. **105**, 212502 (2010).

[45] F. E. Close et al., Phys. Lett. B. **129**, 346 (1983).

[46] O. Nachtmann and H. J. Pirner, Z. Phys. C **21**, 277 (1984).

[47] G. Chanfray, O. Nachtmann, and H. Pirner, Phys. Lett. **B147**, 249 (1984).

[48] F. E. Close, R. L. Jaffe, R. G. Roberts, and G. G. Ross, Phys. Rev. D **31**, 1004 (1985).

[49] K. Saito and A. W. Thomas, Phys. Lett. **B327**, 9 (1994).

[50] I. C. Cloet, W. Bentz, and A. W. Thomas, Phys. Rev. Lett. **95**, 052302 (2005).

[51] I. C. Cloet, W. Bentz, and A. W. Thomas, Phys. Lett. **B642**, 210 (2006).

[52] K. Saito, K. Tsushima, and A. W. Thomas, Prog. Part. Nucl. Phys. **58**, 1 (2007).

[53] I. C. Cloet, W. Bentz, and A. W. Thomas, Phys. Rev. Lett. **102**, 252301 (2009), 0901.3559.

[54] J. Smith and G. Miller, Phys. Rev. C **70**, 065205 (2004).

[55] J. Smith and G. Miller, Phys. Rev. C **72**, 022203 (2005).

[56] J. Arrington and D. Gaskell, spokespersons, Jefferson Lab experiment E03103.

[57] J. Seely et al., Phys. Rev. Lett. **103**, 202301 (2009).

[58] L. W. Whitlow, E. M. Riordan, S. Dasu, S. Rock, and A. Bodek, Phys. Lett. **B282**, 475 (1992).

[59] J. Arrington, F. Coester, R. J. Holt, and T. S. H. Lee, J. Phys. **G36**, 025005 (2009).

[60] A. Accardi et al., Phys. Rev. D **81**, 034016 (2010), 0911.2254.

[61] A. Accardi, W. Melnitchouk, J. Owens, M. Christy, C. Keppel, et al., Phys. Rev. D **84**, 014008 (2011).

[62] J. Arrington, J. Rubin, and W. Melnitchouk, Phys. Rev. Lett. **108**, 252001 (2012).

[63] L. L. Frankfurt, M. I. Strikman, D. B. Day, and M. Sargsian, Phys. Rev. C **48**, 2451 (1993).

[64] J. Arrington, C. Armstrong, T. Averett, O. K. Baker, L. de Bever, et al., Phys.Rev.Lett. **82**, 2056 (1999).

[65] K. S. Egiyan et al. (CLAS), Phys. Rev. C **68**, 014313 (2003).

[66] K. S. Egiyan et al. (CLAS), Phys. Rev. Lett. **96**, 082501 (2006).

[67] R. Shneor et al. (Jefferson Lab Hall A Collaboration), Phys. Rev. Lett. **99**, 072501 (2007).

[68] R. Subedi et al., Science **320**, 1476 (2008).

[69] N. Fomin et al., Phys. Rev. Lett. **108**, 092502 (2012).

[70] J. Arrington, D. Higinbotham, G. Rosner, and M. Sargsian, Prog. Part. Nucl. Phys. **67**, 898 (2012).

[71] J. Arrington et al., Phys. Rev. C **64**, 014602 (2001).

[72] J. Arrington, Heavy Ion Phys. **21**, 295 (2004), hep-ph/0304213.

[73] G. I. Smirnov, Eur. Phys. J. **C10**, 239 (1999).

[74] V. Burov, A. Molochkov, and G. Smirnov, Phys. Lett. **B466**, 1 (1999).

[75] I. R. Afnan, F. R. P. Bissey, J. Gomez, A. Katramatou, S. Liuti, et al., Phys. Rev. C **68**, 035201 (2003).

[76] C. W. Leemann, D. R. Douglas, and G. A. Krafft, Ann. Rev. Nucl. Part. Sci. **51**, 413 (2001).

[77] J. Arrington, Ph.D. thesis, California Institute of Technology (1998), arXiv:nucl-ex/0608013.

[78] D. Dutta et al., Phys. Rev. C **68**, 064603 (2003).

[79] O. K. Baker et al., Nucl. Instrum. Meth. **A367**, 92 (1995).

[80] H. Mkrtchyan et al., Nucl. Instrum. Meth. **A719**, 85 (2013).

[81] M. Berz, COSY Infinity Version and Reference Manual (1995), NSCL Technical report MSUCL-977.

[82] H. Blok et al., Phys. Rev. C **78**, 045202 (2008).

[83] A. Daniel, Ph.D. thesis, University of Houston (2007).

[84] D. Day and I. Sick, Phys. Rev. C **69**, 028501 (2004).

[85] O. Benhar, D. Day, and I. Sick (2006), nucl-ex/0603032.

[86] N. Fomin, Ph.D. thesis, University of Virginia (2008), arXiv:0812.2114.

[87] P. E. Bosted and M. E. Christy, Phys. Rev. C **77**, 065206 (2008), 0711.0159.

[88] L. W. Mo and Y. S. Tsai, Rev. Mod. Phys. **41**, 205 (1969).

[89] Y. S. Tsai, (1971), SLAC-PUB-848.

[90] S. Dasu, Ph.D. thesis, University of Rochester (1988).

[91] A. Aste and J. Jourdan, Europhys. Lett. **67**, 753 (2004), nucl-th/0403075.

[92] R. Rosenfelder, Annals Phys. **128**, 188 (1980).

[93] J. Arrington, F. Coester, R. Holt, and T.-S. Lee, J. Phys. **G36**, 025005 (2009).

[94] A. Bodek et al., Phys. Rev. D **20**, 1471 (1979).

[95] M. Arneodo, Nuc. Phys. B **364**, 107 (1995).

[96] M. Arneodo, Nuc. Phys. B **487**, 3 (1997).

[97] H. L. Lai et al., JHEP **04**, 089 (2007).

[98] A. Airapetian et al., JHEP **1105**, 126 (2011), 1103.5704.

[99] H. Georgi and H. D. Politzer, Phys. Rev. D **14**, 1829 (1976).

[100] A. Accardi and W. Melnitchouk, Phys. Lett. **B670**, 114 (2008).

[101] A. Accardi and J.-W. Qiu, JHEP **07**, 090 (2008).

[102] I. Niculescu et al., Phys. Rev. Lett. **85**, 1182 (2000).

[103] W. Melnitchouk, R. Ent, and C. Keppel, Phys. Rept. **406**, 127 (2005).

[104] M. Osipenko et al. (CLAS Collaboration), Nucl. Phys. **A845**, 1 (2010).

[105] B. Schmookler et al., Nature **566**, 354 (2019).

[106] See Supplemental Material at [to be inserted] for the EMC ratios from this experiment and the updated SLAC results.

[107] P. Bosted and V. Mamyan (2012), 1203.2262.

[108] S. Dasu, P. deBarbaro, A. Bodek, H. Harada, M. Krasny, et al., Phys. Rev. D **49**, 5641 (1994).

[109] A. C. Benvenuti et al. (BCDMS), Phys. Lett. **B189**, 483 (1987).

[110] P. Solvignon, D. Gaskell, and J. Arrington, AIP Conf. Proc. **1160**, 155 (2009), arXiv:0906.0512.

[111] L. Tao et al. (E140X Collaboration), Z.Phys. **C70**, 387 (1996).

[112] V. Tvaskis, M. Christy, J. Arrington, R. Asaturyan, O. Baker, et al., Phys. Rev. Lett. **98**, 142301 (2007).

[113] V. Mamyan, Ph.D. thesis, University of Virginia (2012), arXiv:1202.1457.

[114] S. A. Alsalmi, Ph.D. thesis, Kent State U. (2019).

[115] M. Christy and C. Keppel, spokespersons, Jefferson lab experiment E02109.

[116] J. Arrington, P. Solvignon, D. Higinbotham, and D. B. Day, spokespersons, Jefferson lab experiment E08014.

[117] S. Malace, M. Christy, D. Gaskell, C. Keppel, P. Solvignon, and H. Szumila-Vance, spokespersons, Jefferson lab experiment E12-14-002.

[118] M. Sargsian, CLAS Note 90-007.

[119] J. Arrington and N. Fomin, Phys. Rev. Lett. **123**, 042501 (2019).

[120] O. Hen, D. Higinbotham, G. Miller, E. Piasetzky, and L. Weinstein, Int. J. Mod. Phys. E. 22, **1330017** (2013).

[121] M. M. Sargsian (2012), arXiv:1210.3280.

[122] J. Arrington, A. Daniel, N. Fomin, and D. Gaskell, spokespersons, Jefferson lab experiment E12-10-008.

[123] G. Petratos, J. Arrington, M. Katramatou, D. Meekins, and R. Ransome, spokespersons, Jefferson lab experiment E12-10-103.